Broad-band near-field ground motion simulations in 3-dimensional scattering media

W. Imperatori[1] and P. M. Mai[2]

[1]*Institute of Geophysics, ETH Zurich, Sonneggstr. 5, CH-8092 Zurich, Switzerland. E-mail: imperatori@tomo.ig.erdw.ethz.ch*
[2]*Division of Physical Sciences and Engineering, KAUST, Thuwal 23955-6900, Kingdom of Saudi Arabia*

SUMMARY

The heterogeneous nature of Earth's crust is manifested in the scattering of propagating seismic waves. In recent years, different techniques have been developed to include such phenomenon in broad-band ground-motion calculations, either considering scattering as a semi-stochastic or purely stochastic process. In this study, we simulate broad-band (0–10 Hz) ground motions with a 3-D finite-difference wave propagation solver using several 3-D media characterized by von Karman correlation functions with different correlation lengths and standard deviation values. Our goal is to investigate scattering characteristics and its influence on the seismic wavefield at short and intermediate distances from the source in terms of ground motion parameters. We also examine scattering phenomena, related to the loss of radiation pattern and the directivity breakdown. We first simulate broad-band ground motions for a point-source characterized by a classic ω^2 spectrum model. Fault finiteness is then introduced by means of a Haskell-type source model presenting both subshear and super-shear rupture speed. Results indicate that scattering plays an important role in ground motion even at short distances from the source, where source effects are thought to be dominating. In particular, peak ground motion parameters can be affected even at relatively low frequencies, implying that earthquake ground-motion simulations should include scattering also for peak ground velocity (PGV) calculations. At the same time, we find a gradual loss of the source signature in the 2–5 Hz frequency range, together with a distortion of the Mach cones in case of super-shear rupture. For more complex source models and truly heterogeneous Earth, these effects may occur even at lower frequencies. Our simulations suggests that von Karman correlation functions with correlation length between several hundred metres and few kilometres, Hurst exponent around 0.3 and standard deviation in the 5–10 per cent range reproduce the available observations.

Key words: Earthquake ground motions; Coda waves; Wave scattering and diffraction.

GJI Seismology

1 INTRODUCTION

The structural complexity of the Earth's interior governs the propagating seismic wavefield at different scales. Scattering represents an important process affecting seismic waves travelling in the Earth. It occurs at many different scales and is determined by Earth's heterogeneities located in the crust (Levander & Holliger 1992; Levander *et al.* 1994; Bean *et al.* 1999) as well as in the mantle (Hedlin *et al.* 1997; Helffrich & Wood 2001; Thybo *et al.* 2003). Coda waves constitute perhaps the most prominent phenomenon due to scattering. Extensive theoretical studies on this topic date back to the pioneering work of Aki (1969) who recognized coda waves as backscattered seismic energy from uniformly distributed scatterers in the Earth's crust. Several theories have been developed to explain in more detail the nature of such waves, including single scattering and multiple

scattering theories (e.g. Aki & Chouet 1975; Sato 1977) and energy transport theory (Wu 1985). These were eventually condensed into the compact scattered wave energy equation of Zeng *et al.* (1991) and Zeng (1993), allowing for multiple *S*-to-*S* energy conversions. Heterogeneities in crust/mantle properties are also responsible for envelope broadening (Sato 1989) and variations in waveform, amplitude and traveltime observed across seismic arrays of different apertures (Flatté & Wu 1988).

The seismic waves scattering is commonly classified in different regimes according to the relative size of the heterogeneities (*a*) and the dominant wavelength (or wavenumber *k*) of the propagating wave, as expressed by the product *ka* (see fig. 2 of Wu & Aki 1988). In more detail, when $ka \approx 1$ (size of heterogeneities comparable to wavelength) incident waves are scattered at large angles relative to the incident direction (large-angle scattering); when $ka \gg 1$ (size of

heterogeneities much larger than wavelength) seismic energy is basically scattered into the forward direction (small-angle or forward scattering). In the latter case, a diffraction parameter Λ, controlled also by the distance L over which seismic waves propagate, define the geometric optic (ray theory) and the diffraction subregimes (Wu & Aki 1988). The most significant scattering effects are thought to be produced in the large angle scattering regime (Wu & Aki 1988).

Due to its importance in seismological observations, scattering has been the subject of numerous deterministic numerical modelling studies (Frankel & Clayton 1986; Roth & Korn 1993; Shapiro & Kneib 1993; Frenje & Juhlin 2000; Nielsen & Thybo 2003, among the others). These studies were mainly targeted towards understanding better the scattering process, and to decipher the characteristics and distributions of heterogeneities in the Earth crust and mantle by comparing synthetic data with available theories or observations. Analogous studies were conducted for seismic imaging purposes (e.g. Martini *et al.* 2001; L'heureux *et al.* 2009). However, due to the large computational demands, high-frequency simulations were generally limited to 2-D models when solving the elastic equation of motion, whereas 3-D models were available only in the acoustic approximation. Recently, regional-scale elastic 3-D simulations were carried out by Hartzell *et al.* (2010) and Pitarka (2009), though the maximum frequency was limited to 1 and 3.5 Hz, respectively. On the other hand, stochastic numerical simulations based on the radiative transfer equation (Gusev & Abubakirov 1996; Przybilla *et al.* 2006) or using the Markov approximation (Saito *et al.* 2002; Sawazaki *et al.* 2011) were carried out to reproduce mean square envelopes of high-frequency waves.

In the framework of ground-motion prediction and earthquake engineering, scattering has been included in synthetic seismograms via so-called hybrid techniques (e.g. Liu *et al.* 2006; Graves & Pitarka 2010; Mai *et al.* 2010). These techniques are computationally efficient, while still approximating the fundamental characteristics of scattered waves, as demonstrated by comparison with observed seismograms and ground motion prediction equations (GMPEs). Their principal limitation is that high-frequency waves, radiated by a potentially complex source, are represented by an essentially stochastic time-series that originates at the source and then travels through the medium unperturbed. The generated coda waves can be interpreted as being exclusively due to the complexity of the rupture process, but are not further affected by seismic scattering during the wave propagation. This aspect has been partially addressed in the method proposed by Mai *et al.* (2010), where the high-frequency Green's functions explicitly reflect the scattering properties of the medium, although they are completely uncorrelated even for close neighbouring stations.

In this paper, we conduct for the first time high-frequency (0–10 Hz) deterministic simulations to study seismic scattering in 3-D heterogeneous Earth crust models, focusing on its influence on the wavefield at short and intermediate distance from the source. We construct several 3-D random media using von Karman correlation functions parametrized based on recent findings (e.g. Dolan *et al.* 1998; Nielsen & Thybo 2006). Our analysis focuses on the properties of coda envelopes and waveform coherence across neighbouring receivers, but also addresses typical ground motion parameters used in the engineering community [peak ground acceleration (PGA), peak ground velocity (PGV) and spectral acceleration (SA)]. Our goal is to explore and quantify the level and variability of ground-shaking due to seismic scattering. In addition, we investigate ground-motion phenomena like the loss of the radiation pattern at high frequencies and the breakdown of the directivity effect.

2 3-D VELOCITY MODELS

Heterogeneities in the Earth are commonly characterized as a superposition of a deterministic velocity model and a spatial random field whose key features are defined by the Fourier transform of the particular correlation function adopted. The band-limited von Karman correlation function is frequently used in both borehole data analysis (e.g. Holliger 1997; Dolan *et al.* 1998) and numerical simulations (e.g. Frankel & Clayton 1986; Hartzell *et al.* 2010), and adopted also in our study. Its corresponding power spectrum is given by,

$$P(k) = \frac{\sigma^2 (2\sqrt{\pi}a)^E \Gamma(\nu + \frac{E}{2})}{\Gamma(\nu)(1 + k^2 a^2)^{(\nu + \frac{E}{2})}}, \tag{1}$$

where k is the wavenumber, Γ the Gamma function and E the Euclidian dimension. The standard deviation of the velocity perturbations is given by σ. Parameter a defines the isotropic correlation distance which in principle could be chosen anisotropic (a_x, a_y, a_z). The Hurst exponent ν controls the spectral decay at wavenumbers larger than the corner wavenumber ($k > 1/a$). This correlation function shows fractal (i.e. scale-invariant) properties at length scales smaller than the correlation distance. For ν equal to 0.5, eq. (1) correspond to the power spectrum of the exponential correlation function.

Unfortunately, only few reliable estimates of the spectral parameters in eq. (1) are available. In borehole analysis, an important source of uncertainty in spectral-parameter estimation is introduced by the data processing, and correlation length estimates can be affected by the limited extent of the boreholes themselves (Dolan & Bean 1997). Considering also studies based on interpreting geological maps, available correlation length values range from metric to kilometric scales, whereas Hurst exponent estimates result between 0.2 and 0.3 (Holliger 1996; Bean *et al.* 1999). Similarly, numerical simulations yield correlation length estimates between several hundreds of metres and a few kilometres and Hurst exponent generally in the range between 0 and 0.3 (Frankel & Clayton 1986; Nielsen & Thybo 2003; Przybilla *et al.* 2009). In their simulations, Frankel & Clayton (1986) explored also Gaussian and exponential correlation functions, but they were found less adequate to match the essential features of scattering phenomena.

In our paper, we explore ground-motion variability by adopting a set of 3-D random velocity models characterized by different correlation length (5 km, 500 and 50 m), Hurst exponent (0.1 and 0.3) and standard deviation (5 and 10 per cent of background velocity), as summarized in Table 1. The resulting 1-point statistics are Gaussian. Notice that the results presented in this paper are always intended as averaged over these three realizations per velocity model. Our models are constructed in the wavenumber domain following the spectral technique of Pardoiguzquiza & Chicaolmo (1993), where the amplitude spectrum derived from eq. (1) is associated with a uniformly distributed random phase (controlled by its seed number). To avoid aliasing, we taper the amplitude spectrum at high wavenumbers using a Hamming window. Following Frenje & Juhlin (2000), we do not scale the obtained discrete standard deviation to the desired continuous value because the discrete standard deviation is naturally smaller than its continuous counterpart due to the loss of lower and higher wavenumbers. Any subsequent rescaling would, thus, produce media with the wrong characteristics. Beside these models, we follow Goff & Holliger (1999) and consider also a 'multiscale' model, that is, a heterogenous velocity model characterized by multiple correlation distances (5 km, 500 and 50 m, in

Table 1. Characteristics of the heterogeneous velocity models used in our simulations. See text for details.

Background velocity (V_s)	Correlation length (a)	Standard deviation (σ)	Hurst exponent (ν)	Realizations per model
	5 km		0.3–0.1	
	500 m		0.3–0.1	
3500 m s^{-1}	50 m	10–5 per cent	0.3–0.1	3
	multiscale		0.5	
Smooth gradient (see eq. 2)	multiscale	10–5 per cent	0.5	3
Sharp discontinuity at $z = 2$ km	multiscale	10–5 per cent	0.5	3

our case), whose spectrum decays as $1/k$ for wavenumbers higher than the lowest corner wavenumber (Table 1). A multiscale model is obtained by summing each distinct random field, having different phase but same Hurst exponent (0.5) and standard deviation (5 or 10 per cent). The model is then normalized such that the final standard deviation of velocity perturbations is equal to the average value found for the three media. Compared to single correlation length models, a multiscale model reproduces the slope-break observed in covariance functions of borehole velocity logs, and thus implicitly considers different origins for crustal heterogeneities, such as changes in lithology, cracks, etc. (Goff & Holliger 1999).

In this work, we use only isotropic media and neglect any directional variability. Although there is evidence for anisotropy (Dolan *et al.* 1998; Nielsen & Thybo 2003), data scarceness and lack of reliable parameter estimation do not permit us to extend our work in this direction.

We first consider a set of generic crustal models in which random velocity perturbations are superimposed onto a constant background shear wave speed of 3.5 km s^{-1}. Example realizations are displayed in Figs 1(a)–(d), showing vertical sections of velocity models with identical seed number but different correlation distance. Notice how the distribution of the velocity perturbations in the multiscale model differs from those of the other models, as a consequence of each random field being initialized with a different seed number. To make our numerical analysis more robust, we generate for each parameter configuration three distinct realizations of the 3-D models using different seed numbers. We then return average results, averaging over these three realizations of earth models. To avoid unrealistic high velocity values close to the free surface, we introduce a second set of models characterized by a depth-dependent background shear wave profile given by,

$$Vs(z) = 3.5 - 1.5\mathrm{e}^{-(0.4z)}. \tag{2}$$

Here, the superimposed random perturbations are scaled at each depth level to maintain the relative standard deviation. For this second set, we consider only the multiscale random fields with a smoothly varying background medium. As before, we generate three different realizations using varying seed numbers. Fig. 1(e) shows a sample vertical profile, with a shallow, lower velocity values as generally observed in proximity of the Earth's surface. Although our model values are substantially higher than those regularly measured in basins, the chosen exponential form of eq. (2) allows us to balance the high computational demands with realistically modelling physical properties of the Earth crust.

Finally, a third set of models is presented. Based again on the multiscale heterogeneities distribution and featuring a prominent seismic interface at 2 km of depth (Fig. 1f), this set is aimed to mimic near-surface sharp velocity contrasts observed in many standard crustal models. These three sets are thought to capture the basic characteristics of wave propagation in complex media. Moreover, for the last two sets we have considered only multiscale random fields since our intent is to explore how scattering phenomena interacts with more complex velocity profiles.

Beside the heterogenous models presented so far, we consider three unperturbed media, for constant, smooth and sharp depth-dependent background velocity. They serve as reference models when comparing synthetics and analysing scattering effects.

In all models, the V_p/V_s ratio is set to 1.7; potential values of V_p higher than 8 km s^{-1} are clipped to avoid unrealistic velocity values for compressional waves in the crust. Density is computed following eq. (1) of Brocher (2005) based on V_p values,

$$\rho(V_p) = 1.6612V_p - 0.4721V_p^2 + 0.0671V_p^3$$
$$- 0.0043V_p^4 + 0.000106V_p^5, \tag{3}$$

implying that density variations are perfectly correlated with V_p and V_s variations. Finally, we note that we do not include intrinsic absorption, i.e. all our simulations are purely elastic. The motivation for this choice is to unambiguously separate coda properties due to seismic scattering in the Earth crust from coda decay rates due to intrinsic wave-energy loss. Our modelling can be easily extended to include a parametrization of Q, which we leave for future work.

## 3 SOURCE REPRESENTATION AND NUMERICAL MODELLING

Previous studies use an explosive source that generates only compressional waves (Frankel & Clayton 1986; Przybilla *et al.* 2006), or incident plane waves (Roth & Korn 1993; Shapiro & Kneib 1993; Frenje & Juhlin 2000) to examine seismic scattering. In contrast, we deploy both point-like and planar seismic shear-dislocations placed in each model (Fig. 1). For the point-source case we consider a pure strike-slip mechanism and a strike value of about 23° to avoid nodal planes to be parallel to the horizontal axes. The moment release is described by the following expression:

$$f(t) = \frac{t}{\tau^2}\mathrm{e}^{\frac{-t}{\tau}}, \tag{4}$$

where τ represents a characteristic time parameter controlling the rate of the displacement increase (Beresnev & Atkinson 1997). Eq. (4) describes a moment-rate function corresponding to the ω^2 spectrum model (Brune 1970, see inset in Fig. 2a).

We select τ such that the corner frequency is around 0.3 Hz, representative of $M_\mathrm{w} \approx 6–7$ earthquakes, assuming constant stress drop of $\Delta\sigma = 3$ MPa (Allmann & Shearer 2009). Initially, we choose a point-source representation at high-frequency to unambiguously isolate the propagation effects due to scattering, without including further intricacies due to source finiteness and potential rupture
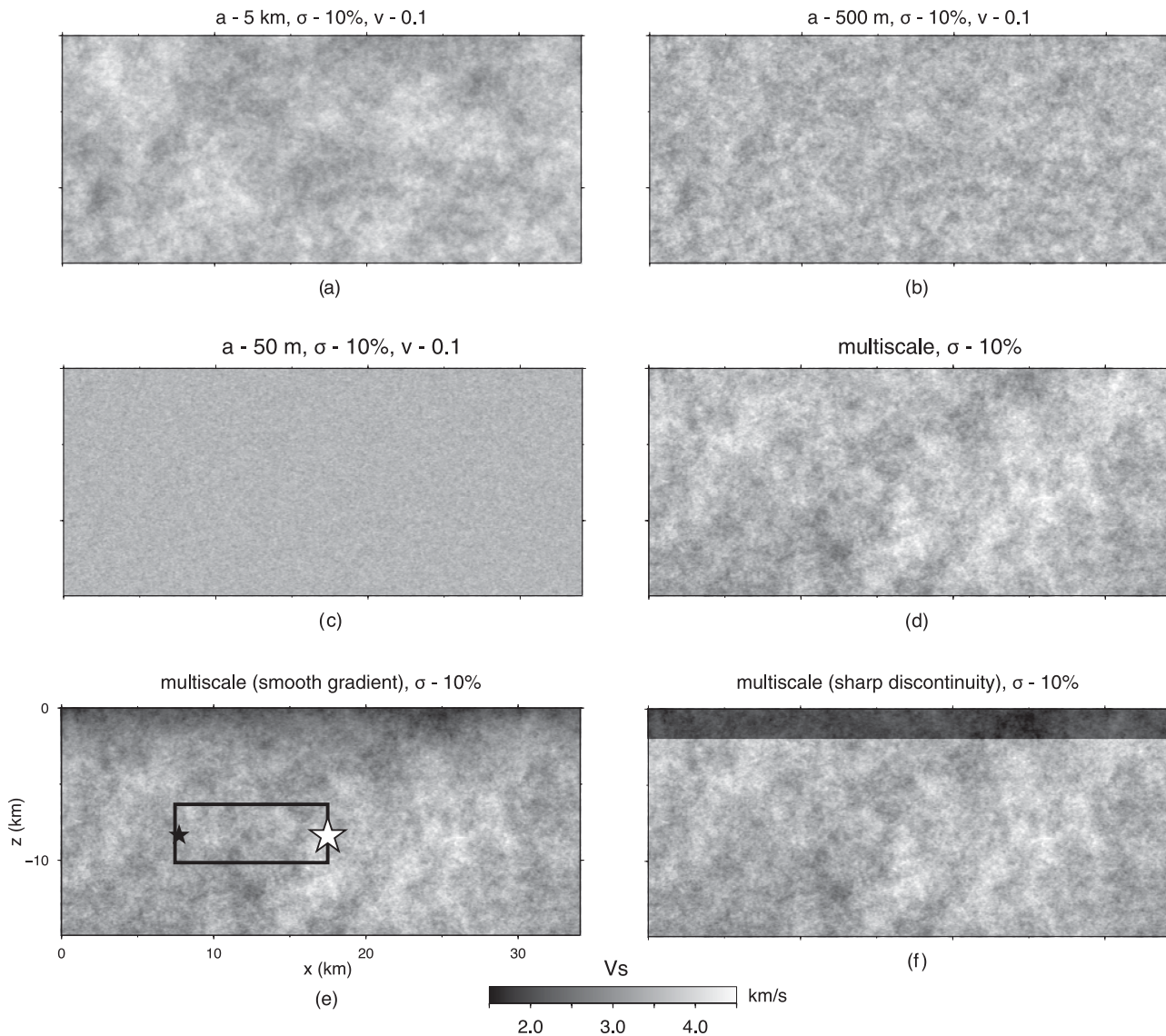
Figure 1. Vertical sections of sample 3-D heterogenous random media realizations used in our numerical simulations (Table 1). Models from (a) to (c) share the same seed number and differ only in terms of correlation distance *a*. The models (d), (e) and (f) are based on three different seed numbers and correlation distances (multiscale models). Model (e) exhibits a background speed-profile gradually increasing with depth (see eq. 2), whereas model (f) presents a strong velocity discontinuity at 2 km depth. The white star indicates the point-source position. The rectangle and the black star represent the extended fault and where its unilateral rupture initiates, respectively.

complexity. We also note that this study focuses on characterizing scattering-induced ground-motion complexities, whereas absolute values of shaking levels are of second-order importance given the source simplicity.

To explore how source directivity is affected by scattering, we introduce a 10 km long, 4 km wide strike-slip finite-source (black rectangle in Figs 1e and 2a). This fault model is characterized by unilateral rupture and uniform slip, rise-time (0.3 s) and rupture speed (rupture initiates at the black star in Figs 1 e and 2a). Each point on the fault is governed by the moment-rate function defined in eq. (4), resulting in a total M_w 5.7. We consider both subshear and super-shear rupture speed (85 and 160 per cent of the background shear wave speed, respectively), and force the rupture to be unilateral to maximize the directivity effects.

These two source representations are undoubtedly characterized by typical signatures: as we will discuss later in detail, the point-

source creates a strong, spiky acceleration peak in the time-series. Its origin can be traced back to the moment-rate function, that releases all the energy during the first 2 s (Fig. 2a). On the other hand, the extended-source resembles a Haskell fault model and, therefore, does not radiate high-frequency energy, consistent with recent findings from rupture dynamic studies (e.g. Pulido & Dalguer 2009; Dunham *et al.* 2011). Although simplistic, these models allow us to efficiently explore first-order seismic scattering effects relevant for ground-motion prediction. More elaborate finite-fault models, including dynamic rupture, require considerably larger computational resources and are subject of future work.

Synthetic seismograms are obtained by numerically solving the equation of motion by means of a 4th-order finite-differences (FD) method (Olsen *et al.* 2009). At zero depth (*z* = 0), free-surface boundary conditions are applied. Calculations are carried out up to a nominal frequency of 10 Hz. Given the lowest shear wave speed

(a)

(b)
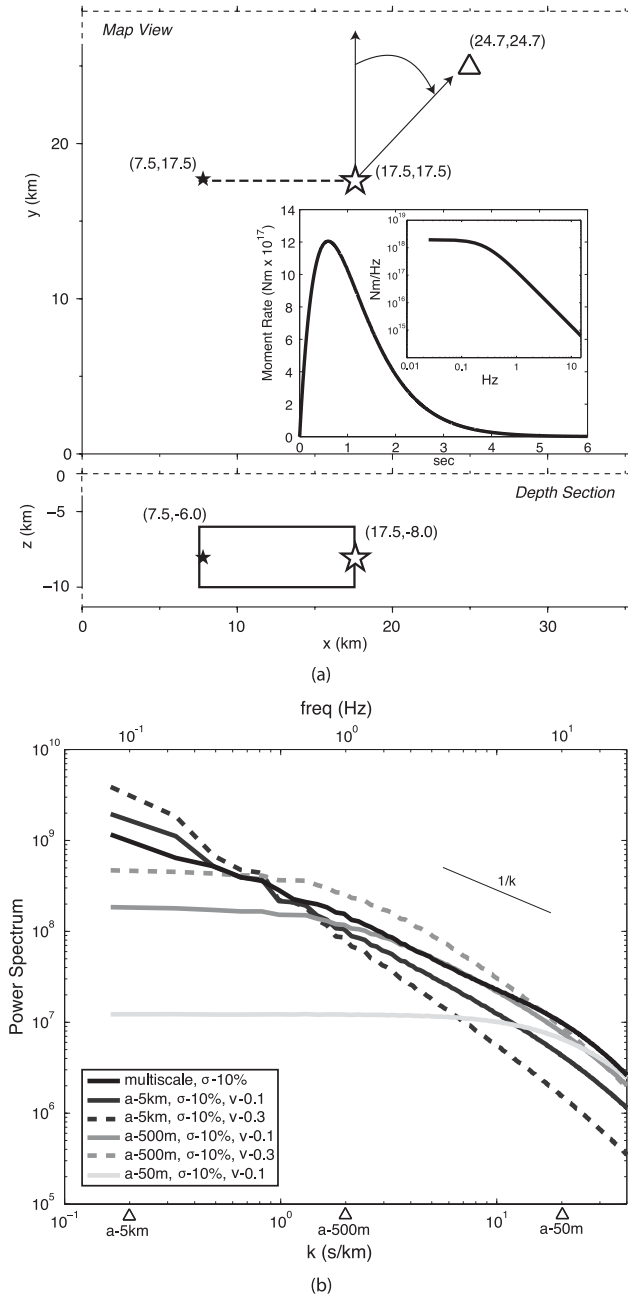
Figure 2. Panel (a): Sketch showing the geometrical setting of our numerical simulations. White star: point source; black star: rupture nucleation point for the extended fault; rectangle: extended fault; black dashed line: extended fault surface projection; white triangle: reference receiver for synthetic seismograms shown in Figs 3 and 10. The azimuthal angle θ is defined as shown. The inset displays the ω^2 moment-rate function describing the energy release for the point-source along with its amplitude spectrum. Each point on the extended fault is characterized by an ω^2 moment-rate function. Panel (b): 1-D-power spectra of selected heterogeneous 3-D media. The lower horizontal axis refers to wavenumbers, the upper horizontal axis to frequency (assuming an average $V_s = 3.5$ km s^{-1}). White triangles on the k-axis indicate corner wavenumbers for single correlation length media. The black thin line represents k^{-1} decay.

in our models, we set a grid-spacing of d$x = 25$ m. As shown by Frenje & Juhlin (2000), a grid-spacing equal to or smaller than the correlation distance guarantees that the original characteristics of the medium are preserved.

To avoid numerical instability at the absorbing boundaries due to the presence of medium inhomogeneities, we embed our media in an unperturbed region of about 100 gridpoints. At each depth level, this region is characterized by a wave speed equal to the average wave speed of the heterogeneous medium at the corresponding depth level. Moreover, although our computational domain extends 40 km along the horizontal direction and 15 km in depth, we analyse ground motion only in a 35×10 km^2 subvolume to reduce effects of wave reflections at imperfectly absorbing boundaries.

4 SCATTERED WAVEFIELD: POINT-SOURCE CASE

In the following section, we analyse the effects produced by scattering on the near-source ground motion in terms of coda waves, radiation pattern distortion, energy partitioning, peak ground motion parameters and waveform similarity. These aspects are of great interest in strong ground motion seismology, and we investigate their sensitivity to different heterogeneity distributions. Our analysis in this section is, therefore, limited to crustal models characterized by uniform background velocity and using a point-source representation. A further analysis considering more complex velocity models and extended source models is reported in the next sections. It should be noticed that, unless differently indicated, the results presented in this work are averaged over the three realizations per velocity model for obtaining unbiased results (see Table 1).

Fig. 3 displays three-component acceleration synthetics for the media reported in Figs 1(a)–(d) at a receiver located on the free surface at 10 km from the epicentre (see Fig. 2a). Seismograms calculated for the homogeneous medium with
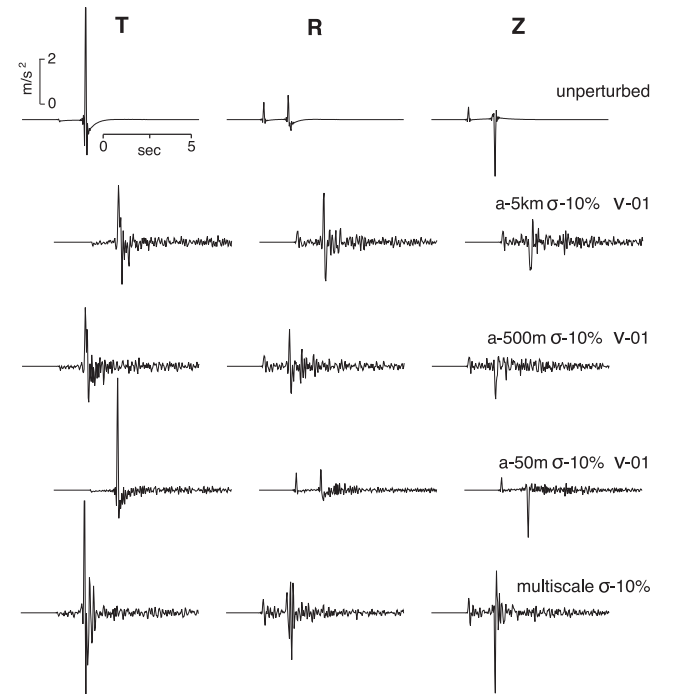
Figure 3. Sample three-component acceleration time-series computed for media **a**–**d** of Fig. 1 at a receiver 10 km away from the epicentre (see white triangle in Fig. 2a). First row shows reference synthetics for the corresponding homogeneous medium. All seismograms, sharing the same horizontal and vertical scale, are arbitrarily shifted for better visualization.
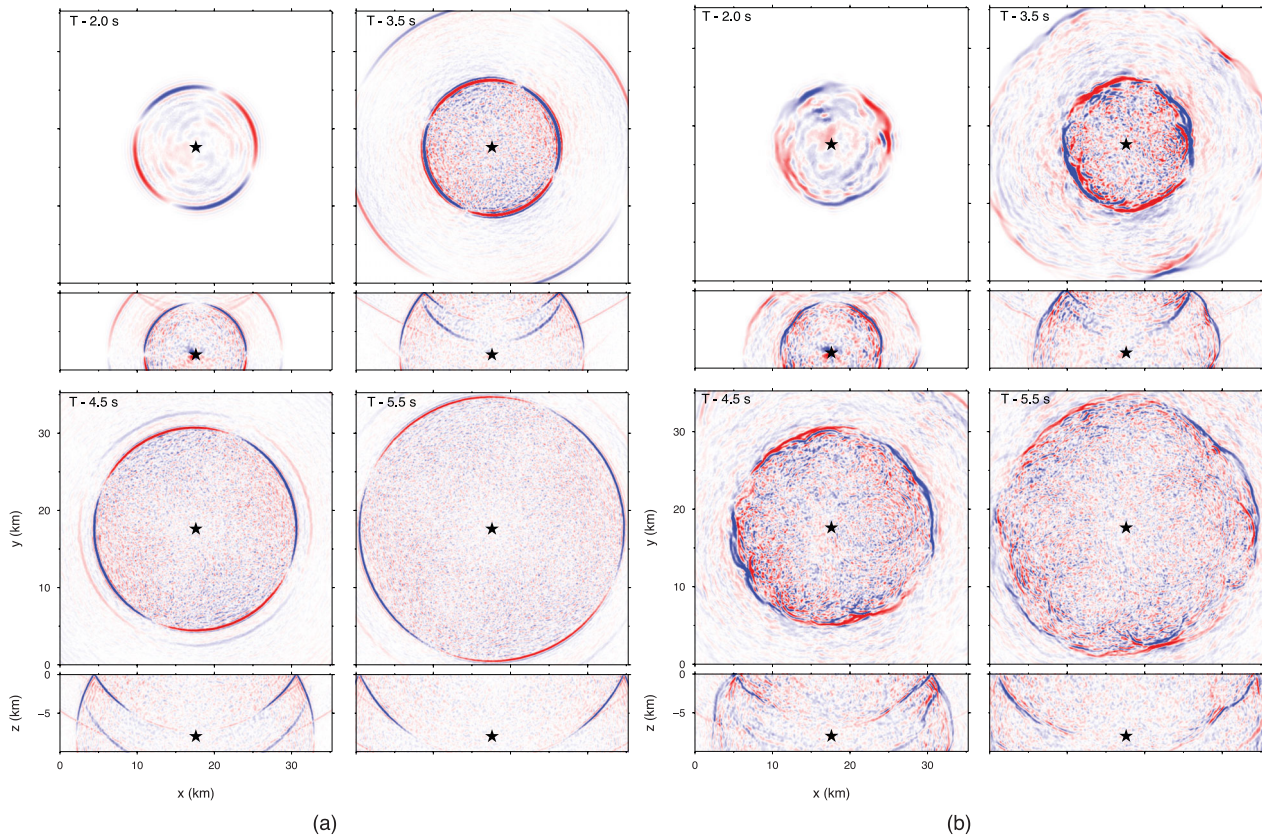
Figure 4. Vertical-component acceleration snapshots for heterogeneous media with (a) 50 m and (b) 5 km correlation length (Figs 1c and 1a), respectively. Snapshots are taken at 2.0, 3.5, 4.5 and 5.5 s after rupture. The point-source position is indicated by the black star. Both map view and vertical section are shown. The vertical plane is parallel to the *x*-axis and cuts the *y*-axis at 16 km. All panels are shown with same amplitude scale.

constant background speed only show direct *P*- and *S*-waves arrivals due to the medium's simplicity and the relatively short source–receiver distance. Synthetics for heterogeneous media conserve the strong *S*-wave phase, especially visible in the transverse component due to the strike-slip mechanism of the source (simulations for different focal mechanisms confirm this observation). Moreover, the absence of sharp, strong velocity discontinuities prevents important wave conversion and reverberation phenomena, potentially able to reduce main peak amplitudes. Coda waves are strongly excited, with intensities that depend on the medium e.g. the 50 m correlation length case reveals the lowest coda amplitudes.

Relative coda amplitudes are also visible in Fig. 4, in which we show snapshots of acceleration for the free surface and a vertical plane close to the source (for brevity only the vertical component for two cases is illustrated; animations for other media and finite-fault rupture can be found in the e-supplement). These snapshots clearly show the scattering associated with each model, and the corresponding complex effects on the wavefield. It is possible to appreciate the difference in wavelength of scattered *P*- and *S* waves. The 5-km correlation length model presents a strong main wave front distortion, due to the relevant heterogeneity size. We also observe particularly complex waveform patterns, just behind the main wave front, resulting from reflection, diffraction and multipathing phenomena. In contrast, the 50 m correlation length model, due to the size of the velocity inhomogeneities, presents less developed scattered waves and a wave front substantially unperturbed. All snapshots, however, reveal how scattering extends the ground-motion duration by exciting coda waves.

4.1 Coda waves analysis

A quantitative estimation of coda waves excitation can be achieved by calculating the relative energy of coda waves (EC) for each component,

$$EC = \frac{\int_{t_s+1.0}^{2t_s} x(t)^2 \, dt}{\int_0^{2t_s} x(t)^2 \, dt}, \qquad (5)$$

where t_s indicates the *S*-wave arrival time and $x(t)$ the time-series. As indicated, we compute the integral considering the energy in a time-window beginning immediately after the main *S*-wave pulse and terminating at twice its value, thus including only the early coda (Sato & Fehler 1994). The 1.0 s value corresponds roughly to the main *S*-wave pulse width in acceleration. Eq. (5) hence expresses the energy contribution of the early coda relative to the first 2 t_s s of the seismic trace. Our analysis is limited to early coda because it is of primary interest in strong ground-motion simulations respect to late coda. Moreover, the maximum time of our simulations is not sufficient for an adequate late coda analysis over in most distance ranges.

In addition, we compute normalized seismogram envelopes as follows:

$$y(t) = \frac{\text{abs}[x(t)] + j^* H[x(t)]}{\max\{\text{abs}[x(t_s)] + j^* H[x(t_s)]\}}, \qquad (6)$$

where j^* is the imaginary unit, H the Hilbert transform and t_s the *S*-wave arrival time. Envelopes can provide a qualitative overview on the character of the coda decay. We compare values obtained from our synthetic data with those derived from the multiple
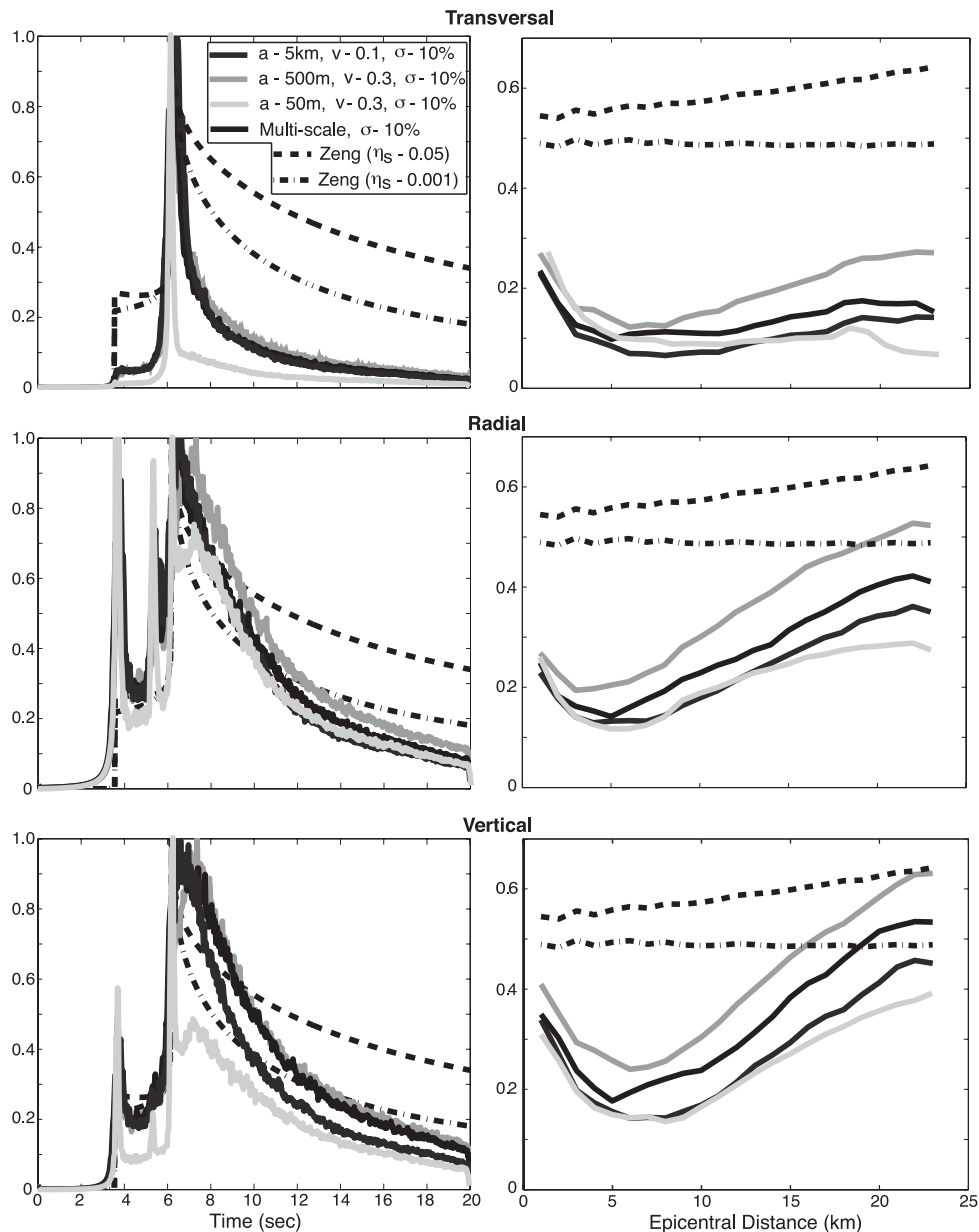
Figure 5. Normalized acceleration envelopes (left-hand column) and EC integral values (right-hand column; see eq. 5) for the three components of motion for different random media, averaged over epicentral distance. Envelopes are computed only at 20-km epicentral distance, whereas EC integrals are reported at several distances. Dashed and dashed-dotted black lines represent envelopes and EC integral values for media with isotropic point-like scatterers characterized by high ($\eta_s = 0.05$) and low ($\eta_s = 0.001$) scattering coefficients, according to the multiple shear-to-shear backscattering theory (Zeng 1991).

shear-to-shear (*S*-to-*S*) backscattering theory (Zeng *et al.* 1991; Zeng 1993; Zeng *et al.* 1995). Following eq. (1) of Zeng (1991), we compute the expected energy integrals (5) and coda envelopes for an isotropic impulsive source in a bounded medium with uniformly distributed isotropic scatterers. We consider both low (0.001 km^{-1}) and high (0.05 km^{-1}) scattering coefficient η_s (Zeng *et al.* 1991; Mena *et al.* 2010), neglecting intrinsic attenuation ($\eta_i = 0$). The hybrid broad-band technique of Mai *et al.* (2010) is based on the same scattering theory, and hence comparisons between theoretical and numerical results are of great interest.

Fig. 5 displays synthetic envelopes (left-hand panel) and EC integrals (right-hand panel) for each component of motion for receivers

at the free surface. Results are averaged over epicentral distance. Note that though EC integrals are reported for the whole distance range, envelopes are shown only for those receivers at 20 km epicentral distance at which coda waves are more fully developed. For each correlation length, we show results for Hurst exponents and standard deviations returning values closest to the corresponding theoretical ones.

All EC integral plots show a characteristic rapid decrease at short epicentral distances (between 0 and 10 km) and a regular increase immediately afterwards. The location of this minimum roughly correspond to the distance where the direct source radiation is maximized, and hence varies according to depth and mechanism

of the source. At very short epicentral distance (<3 km) the scattered energy contribution is rather important, since direct waves are very weak (vertical null axis).

On the other hand, the increasing EC values trend derives from the progressively more important scattering phenomena at the expense of the travelling direct waves. As a general trend, we find that short (50 m) correlation length media generate less coda waves than the others, especially at larger distances. Such effect is even more pronounced for small Hurst exponent values. Multiscale and 500-m correlation length media (at high Hurst exponent) are associated with the highest amplitudes of coda waves instead. We conclude that coda waves generation is very sensitive to the spectral properties of the medium, these being controlled by both correlation length and Hurst exponent.

A more profound understand of this finding can be obtained examining Fig. 2(b), showing 1-D power spectra for some of our heterogeneous media. For $a = 5$ km media an increase in Hurst exponent (i.e. faster power-spectral fall-off) corresponds to lower spectral amplitudes, except at low wavenumbers. The opposite behaviour is found for media with shorter correlation lengths, $a = 500$ m and $a = 50$ m (the latter not reported in the plot). Since velocity perturbations of the medium are proportional to power spectral amplitudes, this analysis provides an intuitive first-order understanding on the relative scattering energy expected in each wavenumber (or frequency) range.

Similar conclusions can be drawn from envelopes in Fig. 5. The apparently less developed coda waves in the transverse component are a consequence of the particular focal mechanism, producing strong peak values in this direction of motion (an analogous phenomenon exists for *P* waves in the radial component). This is confirmed when EC integrals (eq. 5) are computed putting all three components in the denominator limiting the integration to the interval $(t_s + 1.0, 2t_s)$: in this case, values are roughly constant for each component and close to 0.33 for the whole distance range.

A comparison with envelopes and EC integrals as predicted by the backscattering theory of Zeng *et al.* (1991) reveals some differences (Fig. 5). The most notable is represented by the coda decay, clearly observable in the radial and vertical components: whereas theory predicts a gradual decay immediately after the *S*-wave peak, synthetic envelopes show a faster decay in the early coda section. This difference is less pronounced at the largest arrival times (i.e. envelopes tend to be parallel). In this context, another discrepancy is represented by the broader coda just after the *S*-wave arrival observable in the synthetic envelopes (radial and vertical components), which cannot be ascribed to the finite source-time function used in this work, since its duration in acceleration is short (see the 50-m correlation length case, where the *S*-wave pulse is well preserved). We also note how EC integrals computed for synthetics envelopes are comparable to theoretical values only at large epicentral distances, particularly for the multiscale and $a = 500$ m ($\upsilon = 0.3$) models with 10 per cent standard deviation.

Two concurring factors come into play to partially explain the differences between theoretical and simulated coda decay: first of all, the multiple shear-to-shear backscattering theory considers an impulsive isotropic source, characterized by a white-noise spectrum, whereas our source generates a distinctive radiation pattern and a finite-duration omega-squared spectral decay. Thus theoretical envelopes neglect near-source effects related to the radiation pattern and may include scattered energy that is not contained in our synthetics. At the same time, the theoretical coda-decay is based on the assumption that random scatterers are uniformly distributed and

act as local point-like scatterers (Mai *et al.* 2010), independent of the product *ka* fundamental in our simulations. It is, therefore, conceivable that the theoretical predictions tend to generate stronger seismic scattering than the numerical simulations. Moreover, the theoretical model of Zeng *et al.* (1991) considers only backscattering while our numerical simulations encompass different scattering regimes. New theoretical coda decay based on forward scattering is shown to be in better agreement with our simulated coda decay (Y. Zeng, personal communication, 2012).

4.2 Distortion of the radiation pattern

The observed distribution of peak ground parameters, like PGA, is generally assumed to be almost isotropic, i.e. not showing the characteristic four lobes even in case of a small causative faults. A number of studies have investigated this aspect (e.g. Liu & Helmberger 1985; Takenaka *et al.* 2003) and, although in some cases radiation pattern can be still observed even at high frequency (Vidale 1989; Sawazaki *et al.* 2011), there is evidence for a transitional regime (around 1–4 Hz) between the deterministic four lobes and the stochastic isotropic pattern (Pulido & Kubo 2004). Recently Takemura *et al.* (2009), analysing aftershocks of the 2000 western Tottori earthquake recorded by the dense Japanese KiK-net, have shown that the collapse of the apparent *S*-wave radiation pattern is mainly controlled by the travel distance, especially for frequency higher than 2 Hz. At the same time, it has been suggested that the source term may play only a marginal role in the distortion of the radiation pattern, at least for events smaller than M_w 5.5 (Takemura *et al.* 2009).

In this section, we investigate how heterogeneous models interfere with the radiation pattern following the approach of Takemura *et al.* (2009). We evaluate the correlation coefficient *r* of the root-mean-square quantity A_T, defined as,

$$A_T = \frac{|T|}{\sqrt{R^2 + T^2}}, \tag{7}$$

where *T* and *R* are the maximum peak values computed from acceleration synthetics in a 5 s time-window starting from the *S*-wave arrival in the cylindrical transverse and radial component, respectively. Eq. (7) is calculated at different frequency bands after bandpassing the time-series with a narrow (1 Hz bandwidth) Butterworth filter. We then compute the correlation coefficient *r* between the apparent *S*-wave radiation pattern for heterogeneous models and the corresponding radiation pattern for homogeneous medium as a function of frequency. Our intent is to compare this quantity with actual values displayed in figs 5 and 6 of Takemura *et al.* (2009) obtained from borehole data. We prefer to use the latter instead of free-field data because our models do not contain very low *S*-wave velocities typical for sedimentary basins. Moreover, as a consequence of the relatively small size of our models, we are forced to restrict our analysis to receivers on the free surface at 17 km from the epicentre, the largest distance able to guarantee full azimuthal coverage. Results are displayed in Fig. 6(a) for those models only, within each correlation length class, that best match the observed values of Takemura *et al.* (2009). In Fig. 6(b) we report the variation of A_T with azimuth θ (see Fig. 2a) at three different frequencies for one of the multiscale media with 10 per cent standard deviation.

The correlation coefficient *r* for our models shows a decay similar to observational data, especially when the latter are restricted to 25-km hypocentral distance (open squares in Fig. 6a). In particular, though values for multiscale, 5 km and 500 m correlation length media are comparable, those for 50 m correlation length media are
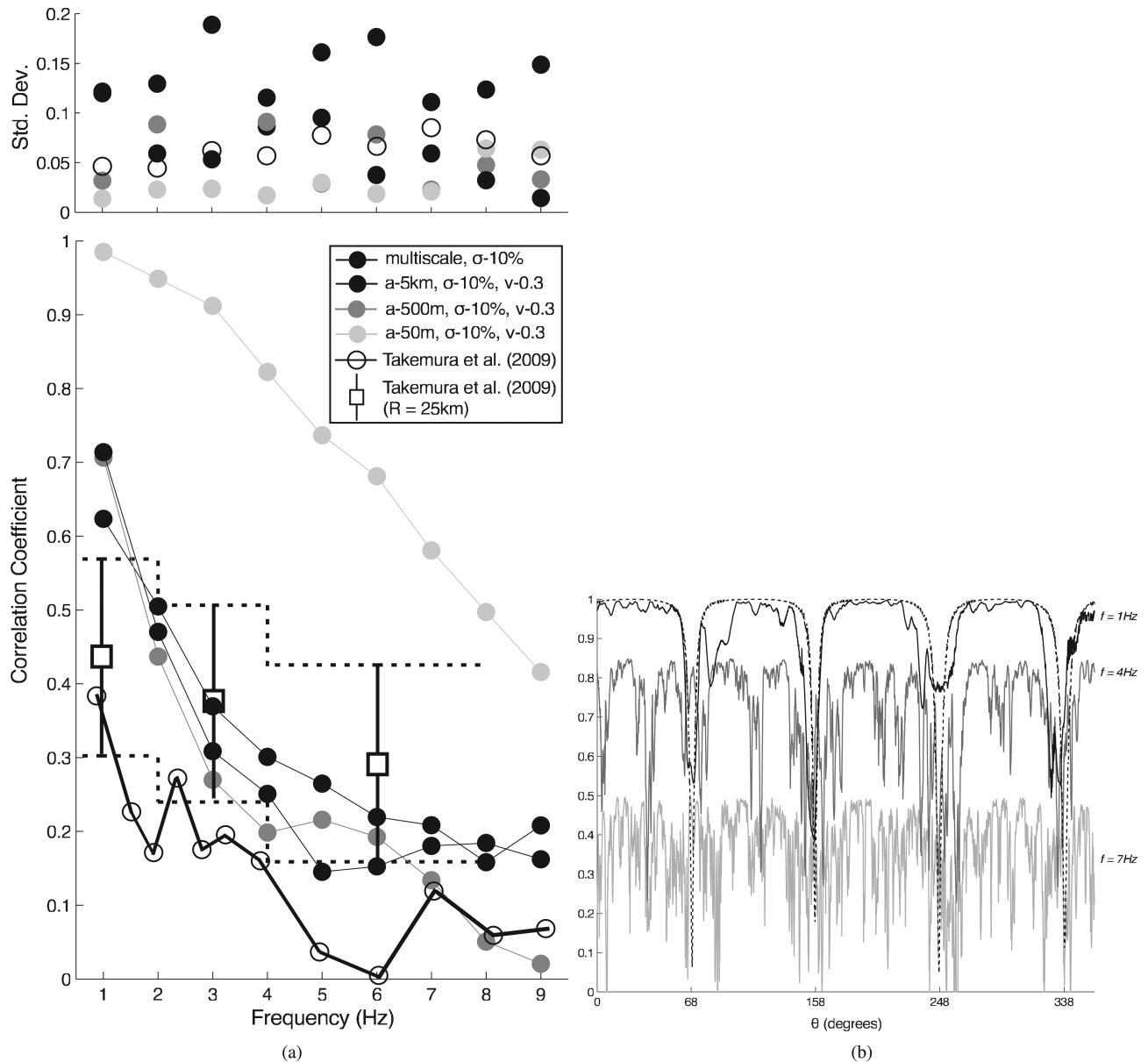
Figure 6. Panel (a): Correlation coefficient *r* between apparent radiation pattern of the *S* wave for a set of heterogenous models, and the reference radiation pattern for the corresponding homogeneous medium as a function of frequency. Only free-surface receivers at 17 km from the epicentre are considered. We plot results only for those models, within each correlation length class, closest to the values observed by Takemura *et al.* (2009,borehole data). Circles in the top panel indicate standard deviation for each frequency band. Panel (b): Example of A_T (eq. 7) variability with azimuth θ at three different frequencies, referred to one of the three multiscale media (with $\sigma = 10$ per cent). Values at $f = 4$ Hz and $f = 7$ Hz are shifted by a constant factor of 0.15 and 0.5, respectively, for better visualization. The dashed black line shows the azimuthal variation in the homogeneous medium.

always higher, indicating the possibility to detect the characteristics four lobes even at high-frequency for this medium. It is worth noting that media with lower Hurst exponent or lower sigma, while still matching empirical data at frequency higher than 5 Hz, present rather high correlation values at low-frequency. This mismatch, slightly visible in Fig. 6(a), may originate from the lack of either large-scale complex features and low-velocity layers in our models: as Takemura *et al.* (2009) pointed out, near-surface structures can disrupt the *S*-wave radiation pattern at frequency lower than 3 Hz.

Moreover, Takemura *et al.* (2009) were able to satisfactorily reproduce the observations at large distance using stochastic 2-D heterogeneous models with correlation length of few kilometres. Examining Fig. 6(b), focused on the multiscale media, it is possible

to notice that at 1 Hz the radiation pattern is well visible with its four *SH* nodal planes. At 4 Hz the apparent radiation pattern is noticeably distorted, being completely unrecognizable (isotropic) at 7 Hz. This eventually confirms the observations of Pitarka (2009) and Takemura *et al.* (2009), who reported a transient radiation pattern regime in the 2–5 Hz frequency band.

4.3 Energy partitioning

Another aspect of interest in strong ground motion is how scattering modifies the spectral energy content of the propagating wavefield. Apparent attenuation is a well-documented phenomenon (Stein & Wysession 2003), and numerous works have pointed out its
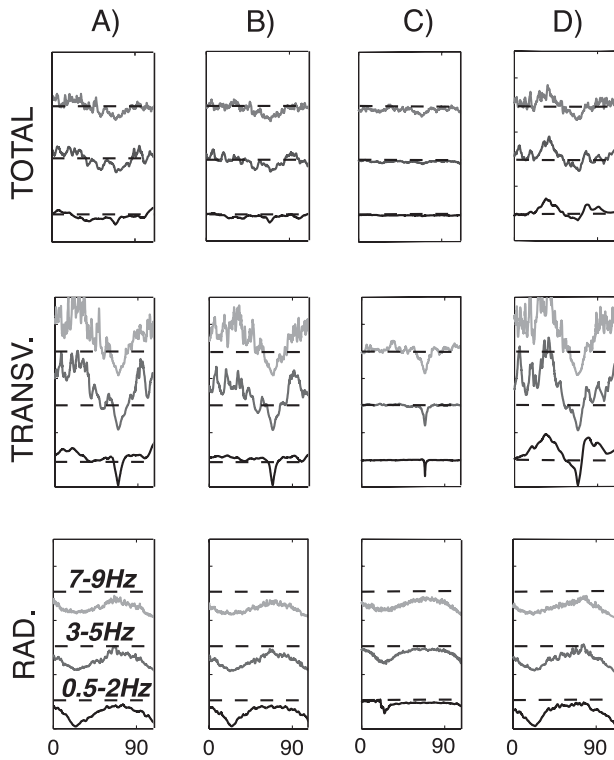
Figure 7. Energy ratios, ER, (see eq. 8) averaged over receivers at about 17 km distance from the epicentre plotted against azimuth θ for transverse and radial components. Due to $\pi/2$ periodicity, values are reported only for a limited azimuth interval. Results arranged in vertical columns refer to: A—$a = 5$ km, $\sigma = 10$ per cent, $\nu = 0.1$ model; B—$a = 500$ m, $\sigma = 10$ per cent, $\nu = 01$ model; C—$a = 50$ m, $\sigma = 10$ per cent, $\nu = 01$ model; D—multiscale, $\sigma = 10$ per cent model. The first row represents the summation of the three components of motion. The frequency bands the ER values are referred to are indicated in bold. Dashed black lines indicate the unity value. See text for details.

frequency-dependent nature (e.g. Mayeda *et al.* 1992). Here, we want to investigate how seismic energy leaving the source is redistributed in its surroundings, and to verify whether there are any preferred directions. Takenaka *et al.* (2003) have found evidence for strong *SV–SH* mixing at high frequency for the direct *S* wave due to the scattered energy redistribution.

In this paper, we do not focus on a particular phase but instead we analyse the energy content over the whole time interval spanned by our synthetics. We compute an energy ratio function (ER), dependent on frequency, in the following way:

$$ER(f) = \frac{\int_{f_c-\delta f}^{f_c+\delta f} U(f)^2 \, df}{\int_{f_c-\delta f}^{f_c+\delta f} P(f)^2 \, df}, \tag{8}$$

where U and P represent the time-series amplitude spectra for unperturbed and perturbed velocity models, respectively. ER is computed for the three components of motion in three different frequency bands ($f_c \pm \delta f$): 0.5–2, 3–5 and 7–9 Hz. Results are summarized in Fig. 7, where we show values only for some representative cases: the multiscale (σ-10 per cent) and the 5 km, 500 and 50 m (σ-10 per cent, ν-0.1) models. We do not display the vertical component since it is accurately represented by the radial one, but it is included in the total summation. Values are plotted against azimuth

(θ) for receivers located on the free surface at 17 km distance from the epicentre.

Eq. (8) expresses the energy variation, in a particular frequency band, determined by scattering phenomena. Despite the relatively short epicentral distance, scattering attenuation would suggest values always greater than 1. Fig. 7 shows instead a more complex pattern especially when scattering is more intense. The transverse component reveals ERs of different degrees of scattering attenuation for all media, increasing as the frequency band increases, but also a rather strong spatial variability with values locally close to unity or even below. It is interesting to observe that these notches are not only located corresponding to the nodal planes, but also in those areas theoretically illuminated by the direct source radiation. We remark also that notches linked to the nodal planes tend to enlarge proportionally to frequency (especially for media with small correlation lengths), thus implying that shorter wavelength radiation is stronger in such areas. The radial (and vertical) component surprisingly is characterized by ER values often below unity, not only corresponding to the nodal planes. This apparently controversial behaviour can be explained by intense *SH–SV* energy mixing happening during the scattering process: as shown by Mossessian & Dravinski (1990), scattering of travelling *P–SV* and *SH* waves by 3-D dipping layers of arbitrary shape is accompanied by strong coupling between *P/SV* and *SH* modes, particularly important in case of incident *SH* waves. This component-dependent effect is generally more pronounced at high frequency, and may mask the scattering energy attenuation (Fig. 7).

When all components of motion are considered simultaneously (first row of Fig. 7), ER at higher frequencies oscillates around unity presenting negative values mainly corresponding to the *SV* and *SH* nodal planes (in the latter case being more prominent). As already pointed out, these negative values are associated with shorter wavelength energy, more prone than longer wavelength contribution to be redistributed by the scattering process. Areas well illuminated by direct source radiation are characterized instead by values slightly higher or equal to 1. It is, therefore, not possible to define a clear effect of the scattering attenuation, probably in part due to the short distance the waves have travelled, also favouring an effective redistribution of part of the radiation leaving the source at different take-off angles.

4.4 Effects on peak ground motion parameters

The influence of scattering on the propagating wavefield can be quantified in terms of peak ground motion parameters. Such parameters, like PGV, PGA and SA are widely used in the seismic engineering community (e.g. Abrahamson *et al.* 2008). Several studies have documented the strong influence exerted by the rupture process on the resulting ground motion variability, both in terms of kinematic (Sørensen *et al.* 2007) and dynamic source modelling (Guatteri *et al.* 2003; Ripperger *et al.* 2008). Recently, Imperatori & Mai (2012) have compared the sensitivity of strong ground motion simulations to source and unperturbed 1-D Earth structure variations. However, the spatial variability at different sites depends also on the heterogeneities of the propagation medium, especially at large distances from the source (Spudich & Chiou 2008). In this section, we investigate how the different spectral characteristics of perturbed media reflect on peak ground motion parameters, thus possibly constituting another factor for ground motion variability even in the near-source region.

Therefore, we compute ratios between PGV, PGA and SA derived for models with heterogeneities and those derived for the reference
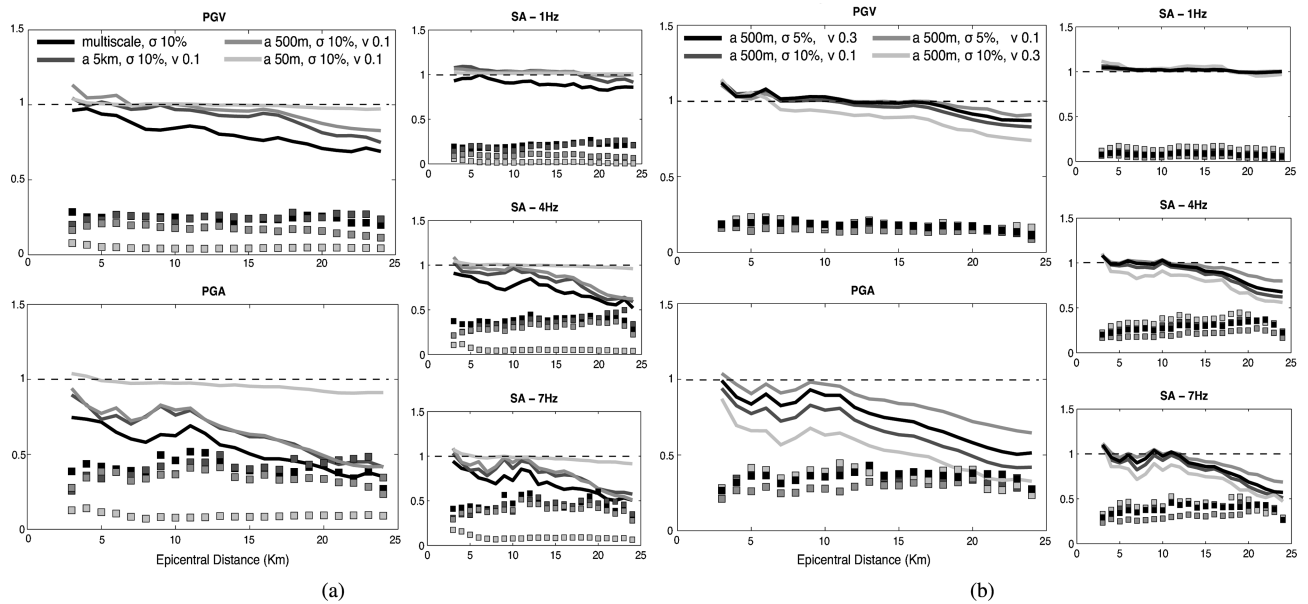
Figure 8. (a) Peak ground velocity (top left-hand panel), peak ground acceleration (bottom left-hand panel) and 5 per cent-damping SA (right-hand columns) ratios computed between each parameter derived for heterogenous media (σ-10 per cent and υ-0.1) and for a reference unperturbed medium. (b) Analogous peak ratios for media with $a = 500$ m. In both cases continuous lines refer to ratios averaged over epicentral distance. Squares indicate standard deviation as a fraction of the corresponding average value. Dashed black line represents unit reference level. All receivers located along nodal planes have been excluded from calculations.

homogeneous model. All receivers within $3°$ of a nodal plane are neglected to exclude values biased by radiation pattern effects. Results are shown in Fig. 8(a). For brevity, we limit our discussion here to those models with 10 per cent standard deviation and Hurst exponent value of 0.1 (except multiscale models), emphasizing eventual differences between models. Beside ratios averaged over receivers at several epicentral distances (continuous lines), we express variability via standard deviation normalized by the corresponding mean value at each distance (squares).

As one could expect values for all parameters display attenuation with distance due to energy redistribution because of scattering phenomena. It is interesting to note that PGV presents a remarkable attenuation (about 20–30 per cent) for most of the models at distances larger than 15–20 km, indicating that also this parameter is sensitive to scattering even at relatively short distances. A major sensitivity is found for PGA, where apparent attenuation is responsible for a decrease of about 50–60 per cent; on the other hand, SA shows frequency-dependent values, which reveal scattering attenuation at frequencies higher than 3 Hz. Although the multiscale, 5 km and 500 m correlation length models are characterized by similar ratios, the 50 m correlation length model generates weak attenuation also at high frequency, implying negligible propagation effects in terms of peak values (but not in terms of coda waves, see Figs 3–5).

When examining variability, we do not observe any distance dependency: values are constant, around 30 per cent for PGV and 40–50 per cent for PGA (again, for SA a frequency-dependence can be found, although values for frequencies higher than 4 Hz tend to stabilize). The standard deviation for 50 m correlation length media is lower as it acts as an effective medium with only weak scattering and energy redistribution in the given frequency range.

We notice also that PGA and SA at 7 Hz for all models (except 50 m correlation length) show an increase in ratio at about 8–10 km, thus, corresponding to the source radiation maximum, where scattering effects are partially reduced since peak values are mostly

determined by direct arrivals. At very short distances (<5 km) PGV ratios are very close to unity or even higher due to the scarce direct energy radiation in the near-source area; this effect is less visible for PGA since the size of this area is reduced.

Fig. 8(b) displays ratios for different media with same correlation length. For brevity, we focus on the 500 m correlation length case only, which can be considered as representative. The most striking feature is found for PGA ratios, where average values for each model are clearly separated. Either a Hurst exponent increase (0.1–0.3) or a velocity fluctuation increase (5–10 per cent) translates into a PGA ratios decrease of about 20–30 per cent at distances greater than 5 km. At shorter epicentral distances this difference changes quickly because of the reduced travelled path. The major effects are caused by the intensity of the velocity fluctuation, whereas changes in the spectral properties of the medium induced by the Hurst exponent (indirectly influencing heterogeneities size) are slightly less important. Such differences are of minor importance for PGV and SA at low frequencies due to the overall reduction of scattering intensity. Similarly, variability values are rather close for all the models; only at high frequency (see PGA and SA at $f > 3$ Hz) some distinctions can be observed. Therefore, the sensitivity to both standard deviation (σ) and Hurst exponent (υ) should be taken into account when simulating ground motion using media with short wavelength heterogeneities.

4.5 Waveform similarity

Scattering-induced spatial variability affects the entire time-series, not only its peak value. Amplitude and arrival time variations across arrays of different aperture have been documented in numerous studies (e.g. Flatté & Wu 1988; Fletcher *et al.* 2006). These studies have underlined the station separation- and frequency-dependent nature of ground motion variability, which is also important in building design (Zerva & Zervas 2002). In this section, we evaluate waveform similarity for the heterogeneous media at three distinct
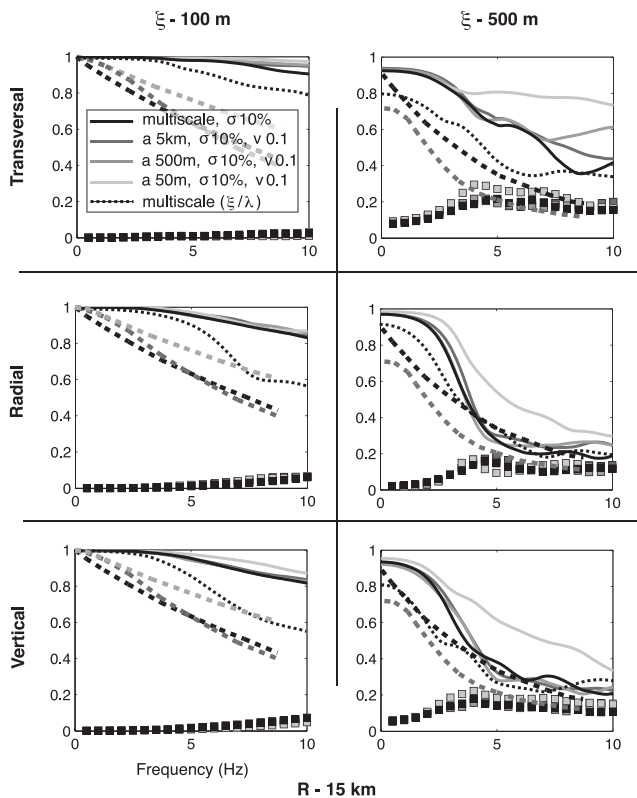
Figure 9. Coherence estimation on transverse, radial and vertical component of acceleration synthetics for selected heterogenous media (σ-10 per cent and υ-0.1). Coherence is averaged over several five-element arrays at different azimuth θ. Results are shown at one epicentral distances R (15 km) and two different station separations ξ (100 and 500 m). Continuous lines represent average values, whereas squares indicate standard deviation. The dotted black line indicates average coherence values for the multiscale case after receivers distance is scaled by wavelength. The dashed black, dark grey and light grey lines represent the coherence empirical model of Hao *et al.* (1989), Harichandran & Vanmarcke (1986) and Schneider *et al.* (1992), respectively.

epicentral distances R (5, 10 and 15 km) and for three different stations separations ξ of 100, 250 and 500 m. Similarity is expressed by means of coherence (Zerva & Zervas 2002) calculated using the Welch's modified periodogram method with 15-points Hamming window over 5-elements arrays. As before, we analyse results in terms of different correlation lengths.

Fig. 9 shows the most representative subset of results, relative to one epicentral distances (15 km) and two station separations (100 and 500 m). Both mean coherence values and standard deviation are displayed. We observe that, in general, the multiscale, 5 km and 500 m correlation length models are characterized by similar coherence levels on all components, although local differences are possible for large station separations at frequencies above 5 Hz, independently of the epicentral distance. We notice also that coherence is slightly higher on the transverse component, probably due to the strong coherent pulse recorded in this direction of motion (see Fig. 3). The highest coherence values are found for the smallest station separation (100 m) and for the 50 m correlation length media: only at high frequency and large epicentral distance the latter shows values close to the other models. At frequencies higher than 3–5 Hz, we find a weak sensitivity on epicentral distance only for large station separations and for radial and vertical components, where the signature of the source is less evident. It is interesting to note that

standard deviation is rather regular, increasing with station separation but with minor differences between random media. Moreover, it has been widely observed in array data analysis (Zerva & Zervas 2002) that standard deviation shows a rough inverse proportionality with coherence.

In Fig. 9, we include some empirical coherence models available in literature (Harichandran & Vanmarcke 1986; Hao *et al.* 1989; Schneider *et al.* 1992). To better compare our data with these models, we scale the receiver separation distance with the average wavelength as coherence is thought to be dependent on wavelength (except at very short distances, see Zerva & Zervas 2002). Here we assume a near-surface shear wave velocity of 1 km s^{-1} for the empirical models and 3.5 km s^{-1} for our heterogenous media. As an example, we present results only for the multiscale case. We observe that our values are generally higher than those predicted by empirical models except at large separation distances (ξ =500 m) and higher frequencies, although distance normalization tends to reduce the misfit. The most important discrepancies are located in the transverse component, probably because of the strong source signature in that particular direction of motion, and are particularly visible for ξ =100 m at low-frequency. We believe that this can be traced back to the lack of near surface, low-velocity layers in our models, which are in fact expected to affect mainly the longest wavelengths.

In this section, we have investigated scattering effects for a point source embedded in heterogeneous media characterized by a constant background velocity with superposition of random perturbations. In the next section, we extend our analysis to simple finite sources to explore the effects on source directivity. In addition, we increase the complexity of the deterministic crustal models by means of depth-dependent velocity profiles.

5 SCATTERED WAVEFIELD: EXTENDED-SOURCE CASE

One of the most relevant observable phenomena induced by source finiteness is directivity that affects both amplitude and duration of near-source ground motions. Such effects are rather strong at low frequency (Somerville *et al.* 1997). As frequency and distance from the source increase, rupture front incoherence and scattering in the propagation media gradually weaken the directivity signature (Day *et al.* 2008; Spudich & Chiou 2008). Although local variations of the rupture process are thought to be the primary source of ground motion variability in the near-fault region (e.g. Mai 2009), the role of scattering is still elusive in this context despite some recent simulation works (Pitarka 2009; Hartzell *et al.* 2010).

To explore how scattering influences directivity, we model a 10 km long, 4-km wide finite-source characterized by unilateral propagation, constant rupture speed and uniform slip and rise-time, thus mimicking the Haskell fault model. Its position is shown in Figs 1(e) and 2(a), including the hypocentre. We consider both subshear and super-shear rupture cases, where the rupture speed corresponds to 80 and 160 per cent of the background shear wave velocity. In Fig. 10, we show acceleration synthetics at a receiver affected by forward rupture directivity (see Fig. 2a). For the subshear case, the fault-normal component is characterized by higher amplitudes than the fault-parallel, as reported by (Somerville *et al.* 1997). The relatively large main pulse visible in the horizontal components, caused by the uniform rupture process, dominates the synthetics for all media choices, whereas scattered seismic waves contribute to the coda complexity depending on the random-media parametrizations. On the other hand, in the super-shear case the
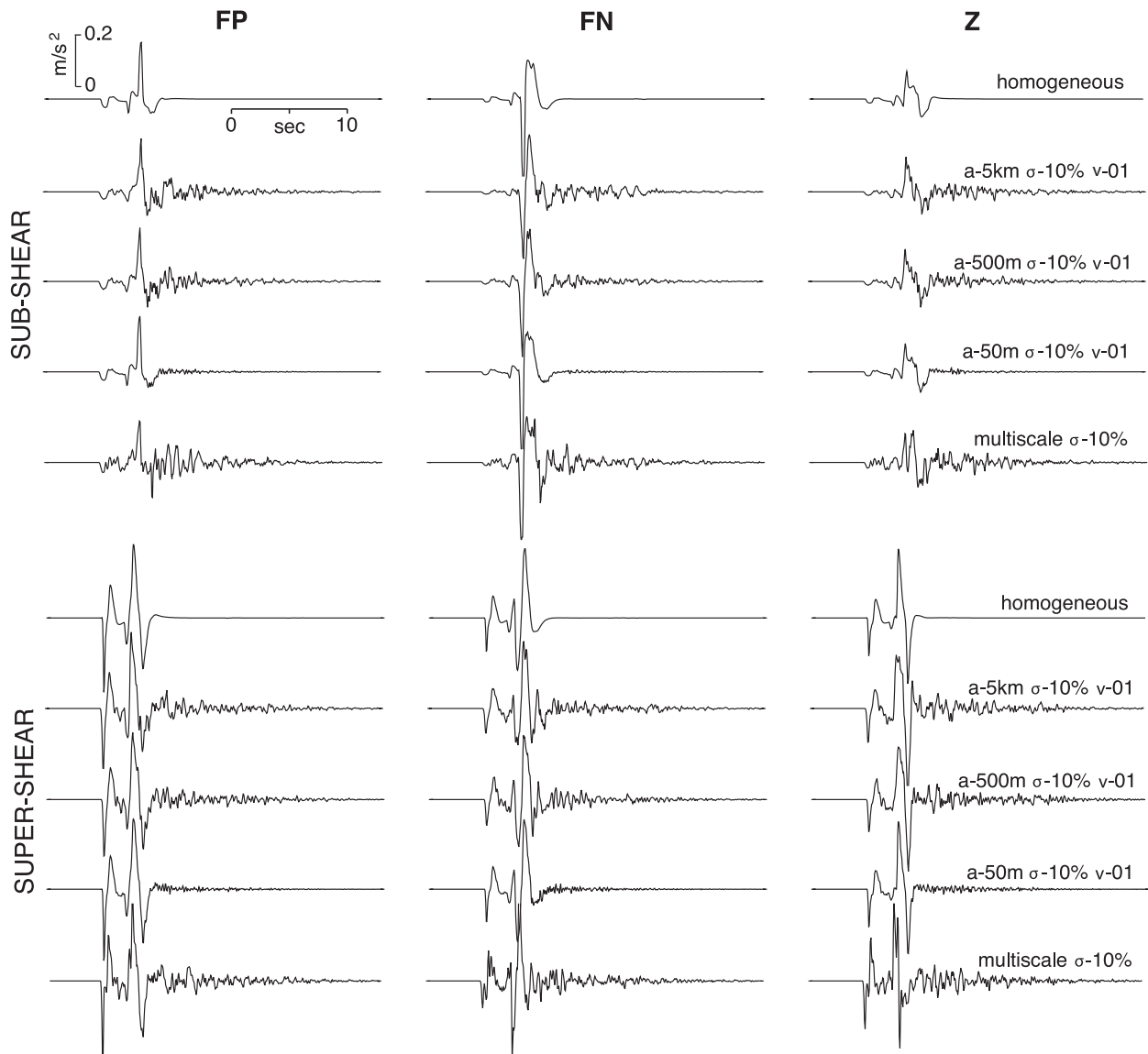
Figure 10. Finite-fault three component acceleration synthetics computed for media **a**–**d** of Fig. 1 at a receiver located at the free surface 10 km from the right-edge of the fault plane (see Fig. 2a). The first row shows reference synthetics for the corresponding homogeneous medium. Both subshear (0.85 V_s) and super-shear (1.6 V_s) cases are shown. All seismograms share same horizontal and vertical scale.

synthetics contain a shorter duration pulse due to the faster rupture process that generates a high-amplitude Mach shear wave, whereas the fault-parallel component amplitude increases strongly (Dunham & Archuleta 2005). Similarly, coda waves in Fig. 10 reflect the difference in frequency content of the two finite-fault models, as super-shear rupture generates also more high frequencies (Bizzarri & Spudich 2008). The relatively large *P*-wave component is due to a rupture speed close to the average *P*-wave velocity in the medium.

In Fig. 11, we show how the horizontal vectorial peak acceleration varies with azimuth θ, at three different frequencies, for one of our media (multiscale, σ-10 per cent) characterized by the most intense scattering effects, allowing us to study how scattering affects directivity in terms of ground motion amplitude. Values are referred to receivers on the free surface at 17 km distance from the right edge of the fault, to assure full azimuthal coverage and normalized to unity. For both rupture models, there is good correspondence at low frequency between the spatial amplitude distribution in the homogeneous and in the perturbed media. Despite the increasing

distortion at higher frequencies, it is possible to observe amplitude differences between receivers in backward and forward direction, especially for the subshear case. These results are in agreement with the recent simulations of Pitarka (2009), obtained for simpler source models at lower frequency, and also with the work of Tan & Helmberger (2010) who found evidence for directivity up to 7 Hz for $M_w < 5$ events in the Big Bear sequence. Similar results were also found by Boatwright (2007) for earthquake clusters of $M_w < 4$ in the San Ramon area (California). At the same time, other studies have reported contrasting observations that directivity effects for large events are found to decrease at short period (e.g. Somerville *et al.* 1997).

A final observation can be made on Mach waves: it has been hypothesized that one reason why such phases are not largely documented relies on the blurring of the Mach wave front generated by multiscale heterogeneities (Bernard & Baumont 2005; Bizzarri *et al.* 2010). Fig. 11 shows, for the homogeneous super-shear case, the presence of an area characterized by high amplitude values at
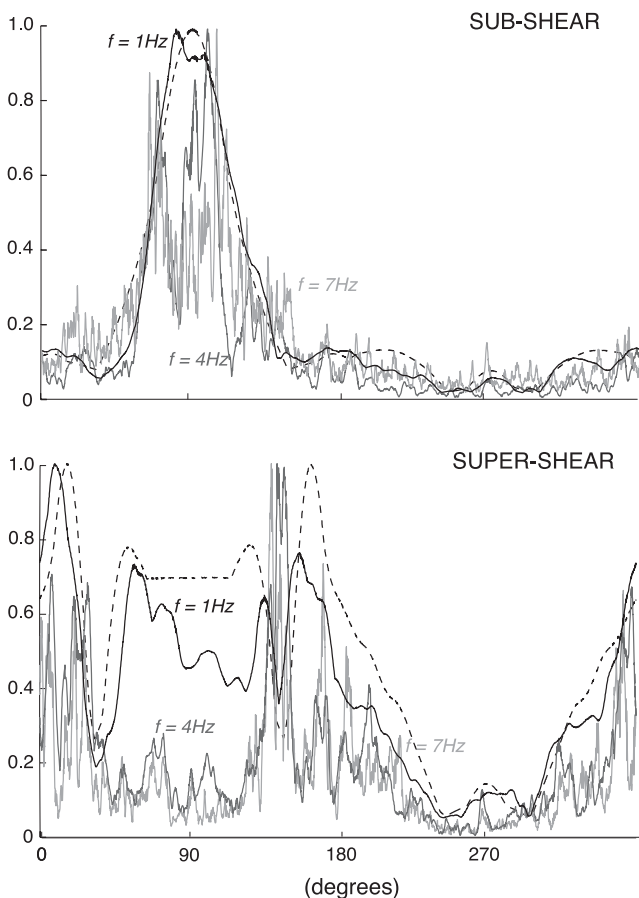
Figure 11. Normalized azimuthal variation of vectorial horizontal peak acceleration for multiscale media ($\sigma = 10$ per cent) at three different frequencies for the finite-fault rupture. As a reference, the dashed black line shows the azimuthal variation in the homogeneous medium.

azimuth angles between $0°$ and $40°$ (and, perhaps, between $140°$ and $180°$). Such high amplitude area, which does not exist in the sub-shear case, is located inside the Mach cone region for the specific rupture speed (Bernard & Baumont 2005). We notice that this area is significantly distorted as frequency increases, being strongly disturbed at already 4 Hz. Therefore, we conjecture that the coherence of Mach fronts is effectively altered by crustal heterogeneities proportionally to frequency, suggesting that velocity time-series might be more appropriate to study these particular phases.

However, it should be noticed that the fault model used in this work is relatively simple. More realistic models, including variable rupture speed and non-planar faults (Dunham *et al.* 2011), will radiate more high-frequency energy and therefore scattering effects on time-series may result even more prominent. Moreover, realistic fault models may clarify the relative contributions of scattering versus source effects on ground-motions. Dynamic rupture simulations in heterogeneous media are currently conducted and will help to extend our work along these directions.

6 SCATTERED WAVEFIELD: VARIABLE VELOCITY PROFILE

All velocity models used in our study so far constitute a first approximation to the complex Earth's upper crust. A more realistic representation requires depth-dependent velocity profiles in which the lowest values are generally recorded in proximity of the free surface. Low velocity horizons are of primary importance also be-

cause they affect the *ka* product and hence wave propagation and scattering regime. Therefore, we extend our simulations for point source to multiscale random media characterized by a smooth velocity gradient (Fig. 1e) and a shallow low velocity layer (Fig. 1f).

The differences introduced by lower velocity horizons are well visible in Fig. 12, displaying acceleration synthetics and the coda/envelope analysis described in Section 4.1. For reference, we include results for the multiscale media with constant background velocity. The most striking feature is represented by strong coda waves, which are more prominently developed for media with lower near-surface velocity values. If a shallow sharp velocity discontinuity is present, an important contribution to coda waves are reverberations of trapped waves. In the limited distance range covered by our simulations, none of the crustal models generates surface waves that could possibly further contribute to early coda (Campillo & Paul 1992). Comparisons with multiple *S*-to-*S* backscattering theory reveal a higher than expected energy content immediately after the direct *S*-wave phase, such that computed and theoretical envelopes are rather different.

However, when evaluating the radiation pattern distortion we do not notice significant differences compared to the constant background velocity case (Fig. 13). The correlation coefficient *r* shows slightly lower values only at low frequency, in agreement with the observations of Takemura *et al.* (2009) for free-field data. The azimuthal variation of *r* for the new models presents shorter wavelength variability, particularly visible at frequencies higher than 4 Hz, resulting from the decrease in *S*-wave speed at the surface. We conjecture that the mismatch in terms of absolute correlation coefficient values at low-frequency is related to the relatively short travel distances involved in our study.

In terms of ground motion parameters, no major differences arise for smooth velocity gradient: as shown in Fig. 14(a), PGV, PGA and SA ratios decay with distance comparably to faster crustal models. On the other hand, the low-velocity layer tends to contrast the apparent attenuation of peak parameters due to scattering, even leading to a local increase with distance. In this case, the shallow layer acts as a waveguide, in which energy is trapped and continuously scattered to create complex propagation effects. As we have noticed in Fig. 12, synthetics associated with this particular medium are characterized by multiple reflections and important coda waves which counterbalance the expected decay of peak parameters. It is worth noticing that our media do not present 3-D deterministic features, like basins, which may further increase waveform complexity.

The reduced dominating wavelength due to shallow horizon and lower wave speeds is also responsible for lower coherence values. As shown in Fig. 14(b), where we report coherence estimates at 15 km from the epicentre, this is visible for both variable velocity profile models at different stations separations. If at short separations the coherence drop is limited to frequencies higher than 4 Hz, for large separations there is a slight drop even at low frequency, bringing our estimates closer to empirical models (Zerva & Zervas 2002). Scaling the receiver separation distance with the average wavelength improves the fit further also for $\xi = 100$ m. From this figure, we notice also that there is no appreciable difference between the proposed variable background velocity models, implying that these models are equivalent in terms of ground motion variability.

7 DISCUSSION AND CONCLUSIONS

In this study, we investigate effects of scattering on near-source ground motion for point sources and extended sources. We describe randomly distributed velocity heterogeneities by a von
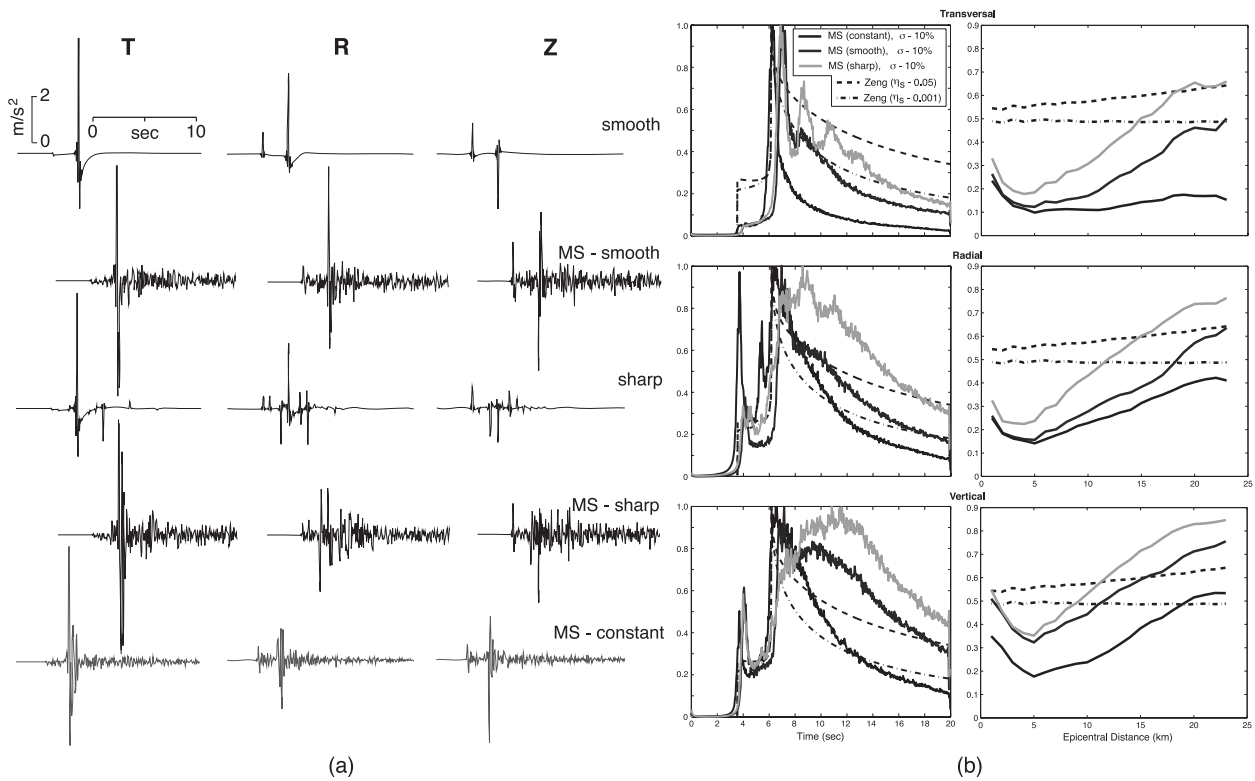
Figure 12. Panel (a): Three component acceleration time-series (relative to the point-source case) computed for multiscale media characterized by a smooth gradient (Fig. 1e) and a shallow low-velocity layer (Fig. 1f), for a receiver located at 10 km distance from the epicentre (see Fig. 2a). For each case, synthetics for the corresponding unperturbed media are also shown. All seismograms, sharing the same horizontal and vertical scale, are arbitrarily shifted for better visualization. As reference, last row displays synthetics referred to the multiscale model with homogeneous background velocity. Panel (b): Acceleration envelopes (left-hand column) and EC integral values (right-hand column; see eq. 5) averaged over epicentral distance for multiscale random media with different background velocity profiles. Envelopes are computed at 20-km epicentral distance, whereas EC integrals are reported at several distances. Values are displayed separately for each component of motion. Dashed and dashed-dotted black lines represent envelopes and EC integral values for media with isotropic point-like scatterers characterized by high ($\eta_s = 0.05$) and low ($\eta_s = 0.001$) scattering coefficients, according to the multiple shear-to-shear backscattering theory (Zeng 1991).

Karman autocorrelation function with varying correlation length, standard deviation and Hurst exponent. We consider both constant and depth-dependent background velocity profiles, examining the cases of a smooth velocity gradient and a sharp discontinuity at shallow depth. Our analysis has revealed complexities in ground motion due to different scattering regimes determined by the crustal models, defined by the product *ka* and the distance *L* over which seismic waves propagate (see fig. 2 of Wu & Aki 1988).

Our simulations are characterized by a source spectrum whose frequency band is flat in acceleration between 0.3 and 10 Hz, an average shear wave speed of 3.5 km s^{-1} (constant background velocity models) and a mean propagation path of about 18 km. Moreover, we need to assume that the correlation length of our random velocity perturbations is directly related to the dominant characteristic scale length of heterogeneities. Although this holds for Gaussian and Exponential media, von Karman media do not contain a characteristic scale for heterogeneities: in this case heterogeneities smaller than the correlation length are present and exhibit a fractal behaviour. However, our assumption can be justified by the fact that these heterogeneities are responsible for velocity perturbations whose amplitude decreases dramatically as the wavenumber increases, controlled by the Hurst exponent (see Fig. 2b). Our heterogeneous media thus cover the whole range of possible scattering regimes: the 50 m correlation length case falls in the Rayleigh scattering zone, with only high-frequency energy results proportional to k^4;

media characterized by 500-m correlation length are dominated by large-angle scattering in which scattering effects are strong; media with 5-km correlation length heterogeneities create large-angle regime (at lower frequencies) and forward scattering regimes (at higher frequencies), where coda waves and scattering attenuation become less intense. The multiscale media, constituting our fourth set of models, consist of different correlation lengths and present characteristics common to both 5 km and 500 m correlation length media (see Figs 1 and 2b).

However, there are two other parameters that affect the scattering process: the standard deviation of velocity fluctuations and the Hurst exponent. Although the former controls directly the scattering intensity acting as a simple scaling factor, the latter enhances/damps different parts of the medium spectrum depending on the correlation length. For instance, synthetics have revealed that different combinations of correlation length, Hurst exponent and standard deviation may produce rather similar results in terms of coda waves energy. As an example, media with *a*-50 m, υ-0.3 and σ-10 per cent are characterized by coda waves whose amplitude is comparable to that found for coda in media with much larger correlation length and smaller standard deviation. What differs, in this case, is the character of the main arrival, being less disturbed for those media with short correlation length. Comparisons with envelopes derived from the multiple *S*-to-*S* scattering theory (Zeng *et al.* 1991), adopted in the hybrid broad-band method of Mai *et al.* (2010), have shown that
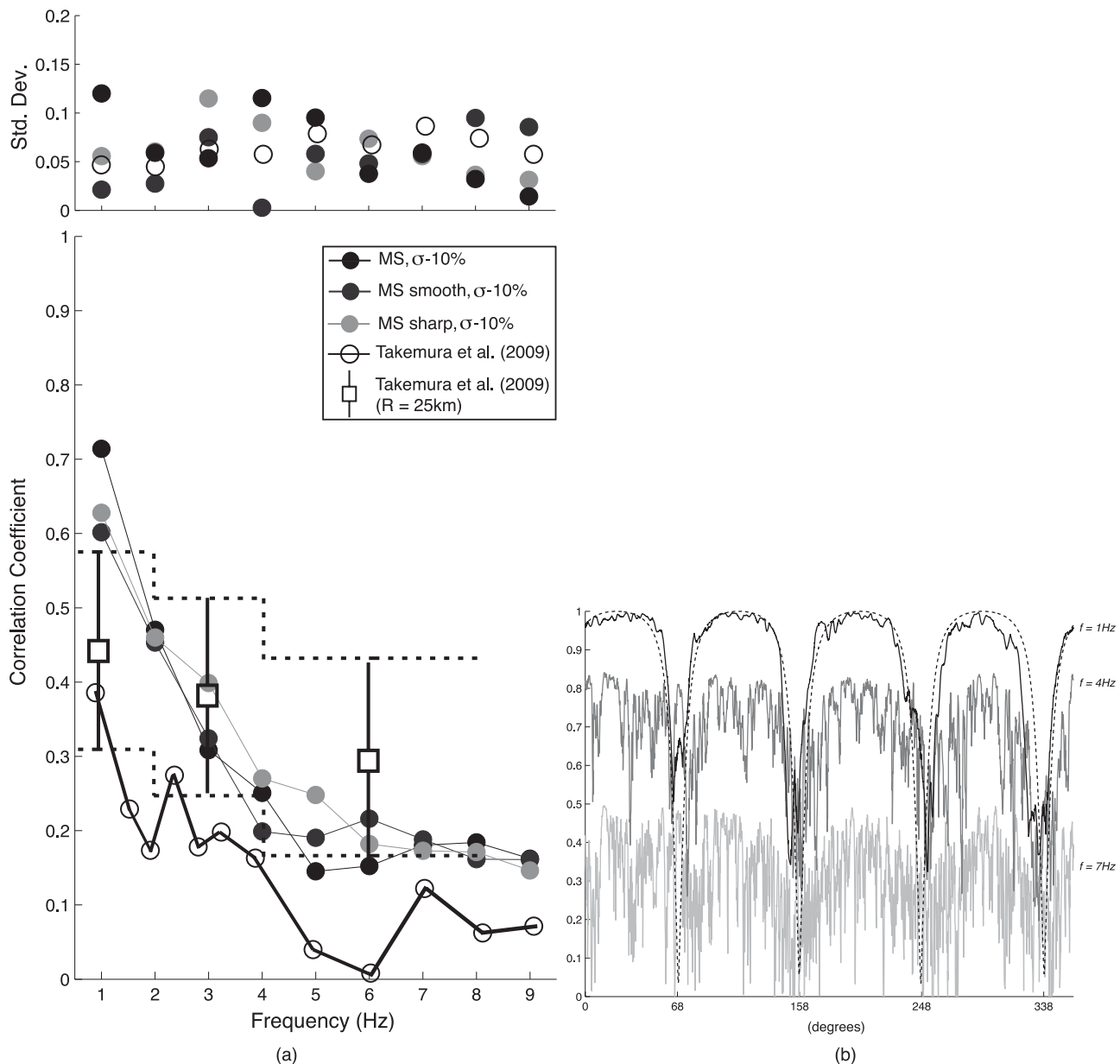
Figure 13. Panel (a): Correlation coefficient *r* between apparent radiation pattern of the *S* wave for multiscale heterogenous models and the reference radiation pattern for the corresponding homogeneous medium as a function of frequency. Only free-surface receivers at 17 km from the epicentre are considered. As a reference, we plot also values observed by Takemura *et al.* (2009,borehole data). Circles in the top panel indicates standard deviation for each frequency band. Panel (b): Example of A_T (eq. 7) variability with azimuth θ at three different frequencies, referred to one of the three multiscale smooth media (10 per cent-σ). Values at $f = 4$ Hz and $f = 7$ Hz are shifted by a constant factor of 0.15 and 0.5, respectively, for better visualization. The dashed black line shows the azimuthal variation in the corresponding homogeneous medium.

actual synthetics contain a more irregular coda decay, far from the expected exponential decay in the early coda section. Such difference is even more remarkable in case of low-velocity horizons.

Another case in which the Hurst exponent plays a major role is represented by ground motion peak parameters, producing variations comparable to those associated with standard deviation (Fig. 8). We find that the apparent attenuation due to scattering may be strong (up to 60 per cent of the original PGA value), as well as the associated variability, depending on the spectral properties of the propagation medium. High apparent attenuation values are not unrealistic, since some studies suggest that scattering is the principal mechanism for attenuation at frequencies below 6 Hz (e.g.

Mayeda *et al.* 1992). PGV values show a minor influence of scattering, although at the largest distances explored in this study a drop of 30 per cent is observed for multiscale and 5 km correlation length media. At the same time, we have found PGV variability values only slightly lower than those derived from dynamic rupture simulations in the near-source region (Ripperger *et al.* 2008). These findings suggest that when computing deterministic synthetic seismograms for ground motion scenarios scattering effects should be considered to produce realistic time-series, even at short distances from the source. Such conclusion corroborates the recent work of Hartzell *et al.* (2010), who studied PGV variability due to velocity perturbations on a regional scale at frequencies lower than 1 Hz. The
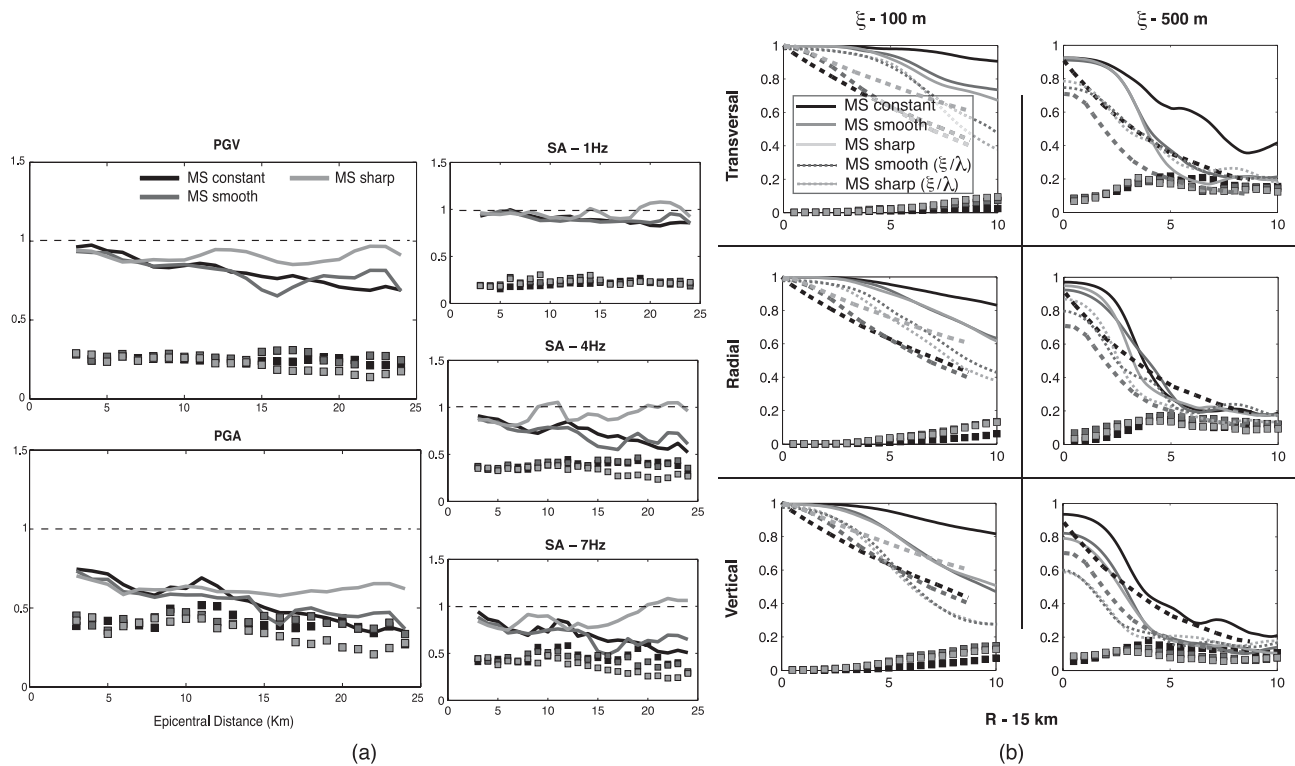
Figure 14. (a) Peak ground velocity (top left-hand panel), peak ground acceleration (bottom left-hand panel) and 5 per cent-damping SA (right-hand columns) ratios computed between each parameter derived for multiscale heterogenous media (σ-10 per cent) and for corresponding unperturbed media. (b) Coherence estimation on transverse, radial and vertical component of acceleration synthetics for multiscale heterogenous media (σ-10 per cent). Coherence is averaged over several five-element arrays at different azimuth θ. Results are shown at one epicentral distances R (15 km) and two different station separations ξ (100 and 500 m). Continuous lines represent average values, whereas squares indicate standard deviation. The dotted lines indicate average coherence values for after scaling receiver distance with wavelength. The dashed black, dark grey and light grey lines represent the coherence empirical model of Hao *et al.* (1989), Harichandran & Vanmarcke (1986) and Schneider *et al.* (1992), respectively. All results are referred to the point-source case (Fig. 2a).

introduction of a smooth velocity gradient does not significantly influence these peak parameters; on the contrary, scattered energy trapped into a low-velocity layer generates complex wave propagation phenomena that reduce the expected peak attenuation. This last aspect could be particularly significant for those studies aimed to determine the amount of intrinsic and scattering attenuation in areas with complex 3-D structures (basins, etc.). From our simulations we conclude that scattering is an important factor affecting ground motion variability in the near-source region, thus effectively competing with the local variations of the rupture process, usually thought to be dominating in the short distance range.

The ground motion variability has been investigated also in terms of waveform coherence, which results independent of the epicentral distance. The lowest coherence is associated with multiscale and 500 m correlation length media, showing a standard deviation generally increasing with frequency. Moreover coherence turns to be extremely sensitive to the product *ka*, and hence to the background velocity profile, whose effects gradually propagate to the lowest frequencies as the stations separation is increased. Our analysis reveals that a realistic simulation of scattering is of primary importance in broad-band ground motion scenarios: even media with small-sized heterogeneities may generate a noticeable waveform variability at high-frequency that needs to be satisfactorily reproduced. We believe it would be of extreme interest to verify how good the most recent hybrid broad-band techniques (e.g. Liu *et al.* 2006; Mai *et al.* 2010) can correctly model this feature.

Moreover, we analyse the effects of scattering on the source signature, both for point-form and extended models. Results from

most models indicate that the radiation pattern distortion becomes important for frequencies higher than 2 Hz, disrupting the characteristic four-lobes at around 5 Hz. On the other hand, we have found that directivity, at least for our specific extended fault models, remains detectable even at relatively high frequency, regardless of the rupture speed. This observation agrees with those of Boatwright (2007), Pitarka (2009) and Tan & Helmberger (2010), who found azimuthal changes in *S*-wave amplitude in a broad frequency range as expression of rupture directivity for events smaller than ours at larger distances. It should be noted, however, that more realistic fault models may lead to different results in this context due to incoherent rupture fronts and larger high-frequency energy content.

Super-shear rupture, by virtue of its intense high-frequency radiation, is subject to more obvious scattering effects: interestingly our simulations show that Mach fronts can be blurred by scattering at intermediate and high frequency even in case of highly coherent rupture. This aspect can represent an explanation for the incoherence of Mach waves invoked by Bizzarri *et al.* (2010) to explain a lack of short period SA amplifications expected for receivers that experienced super-shear rupture (e.g. 1979 Imperial Valley, 1999 Kocaeli and 2002 Denali Fault earthquakes). The loss of the Mach waves signature is expected to be more intense in the truly heterogeneous Earth, and to become progressively more important as the distance from the source increases, suggesting that: (a) velocity time-series should be more appropriate to study these particular waves and (b) it could be difficult to find evidence of super-shear rupture for earthquakes occurring in geologically

complex regions. In particular, this last conjecture implies that super-shear may occur more often than expected in nature, but is rarely observable.

The scattering dependency on the *ka* product is evident in seismograms ERs between unperturbed and perturbed media. Our analysis has underlined that the high-frequency radiation is subject to strong energy redistribution, and that receivers located in areas poorly illuminated by direct source radiation present a relatively higher amount of high-frequency scattered energy. We also find evidence for considerable *SH–SV* energy mixing, which probably constitutes the main mechanism for the radiation pattern distortion as hypothesized by Takenaka *et al.* (2003). These aspects should be taken into account when testing hybrid broad-band ground motion simulation methods. Moreover, numerical simulations suggest that scattering can affect the spectral content of ground motion on a local scale, acting as a redistribution phenomenon only: all the high frequency energy recorded during seismic events originates exclusively from the source.

The intricate sensitivity of scattering to correlation length, standard deviation, Hurst exponent and mean velocity complicates the calibration of our models. Several modelling approaches over the past two decades to retrieve reliable estimates of parameters for specific autocorrelation functions (e.g. Frankel & Clayton 1986; Roth & Korn 1993) were restricted to theoretical models and led to ambiguous results (Shapiro & Kneib 1993). As pointed out by Frenje & Juhlin (2000), even the estimation of scattering attenuation can be problematic in these studies. More recent works involved selected quantities derived from local events, like envelopes (Przybilla *et al.* 2009; Sawazaki *et al.* 2011) or radiation pattern distortion (Takemura *et al.* 2009). We have not performed any inversion or data fit because our models, due to the high frequencies involved and the relatively slow *S*-wave speed, span a limited spatial domain restricted around the near-source region, where direct observations are unfortunately still scarce. Despite this limitation, our work provides some guidelines that, in conjunction with other numerical works and borehole data, could restrict the model parameter space. Following our analysis of coda waves, radiation pattern distortion and waveform coherence, we can affirm that media with correlation length between several hundreds of metres and very few kilometres show characteristics in good agreement with theoretical and empirical models. We have found that Hurst exponent values around 0.3 and standard deviation of velocity perturbation between 5 and 10 per cent improve this fit, as well as the presence of shallow velocity horizons. It is interesting to note that such values are extremely close to those estimated by Holliger & Levander (1992) and Nielsen & Thybo (2003) for the lower crust.

ACKNOWLEDGMENTS

REFERENCES

Abrahamson, N. *et al.*, 2008. Comparisons of the NGA ground-motion relations, *Earthq. Spectra,* **24**(1), 45–66.

Aki, K., 1969. Analysis of seismic coda of local earthquakes as scattered waves, *J. geophys. Res.,* **74**(2), 615–631.

Aki, K. & Chouet, B., 1975. Origin of coda waves: source, attenuation, and scattering effects, *J. geophys. Res.,* **80**(23), 3322–3342.

Allmann, B.P. & Shearer, P.M., 2009. Global variations of stress drop for moderate to large earthquakes, *J. geophys. Res.,* **114**(B01310), doi:10.1029/2008JB005821.

Bean, C.J., Marsan, D. & Martini, F., 1999. Statistical measures of crustal heterogeneity from reflection seismic data: the role of seismic bandwidth, *Geophys. Res. Lett.,* **26**(21), 3241–3244.

Beresnev, I.A. & Atkinson, G.M., 1997. Modeling finite-fault radiation from the ω^N spectrum, *Bull. seism. Soc. Am.,* **87**(1), 67–84.

Bernard, P. & Baumont, D., 2005. Shear mach wave characterization for kinematic fault rupture models with constant supershear rupture velocity, *Geophys. J. Int.,* **162**(2), 431–447.

Bizzarri, A. & Spudich, P., 2008. Effects of supershear rupture speed on the high-frequency content of S waves investigated using spontaneous dynamic rupture models and isochrone theory, *J. geophys. Res.,* **113**(B05 304), doi:10.1029/2007JB005146.

Bizzarri, A., Dunham, E.M. & Spudich, P., 2010. Coherence of Mach fronts during heterogeneous supershear earthquake rupture propagation: simulations and comparison with observations, *J. geophys. Res.,* **115**(B08301), doi:10.1029/2009JB006819.

Boatwright, J., 2007. The persistence of directivity in small earthquakes, *Bull. seism. Soc. Am.,* **97**(6), 1850–1861.

Brocher, T.A., 2005. Empirical relations between elastic wavespeeds and density in the Earth's crust, *Bull. seism. Soc. Am.,* **95**(6), 2081–2092.

Brune, J.N., 1970. Tectonic stress and the spectra of seismic shear waves from earthquakes, *J. geophys. Res.,* **75**(26), 4997–5009.

Campillo, M. & Paul, A., 1992. Influence of the lower crustal structure on the early coda of regional seismograms, *J. geophys. Res.,* **97**(B3), 3405–3416.

Day, S.M., Gonzalez, S.H., Anooshehpoor, R. & Brune, J.N., 2008. Scale-model and numerical simulations of near-fault seismic directivity, *Bull. seism. Soc. Am.,* **98**(3), 1186–1206.

Dolan, S., Bean, C. & Riollet, B., 1998. The broad-band fractal nature of heterogeneity in the upper crust from petrophysical logs, *Geophys. J. Int.,* **132,** 489.

Dolan, S.S. & Bean, C.J., 1997. Some remarks on the estimation of fractal scaling parameters from borehole wire-line logs, *Geophys. Res. Lett.,* **24**(10), 1271–1274.

Dunham, E.M. & Archuleta, R.J., 2005. Near-source ground motion from steady state dynamic rupture pulses, *Geophys. Res. Lett.,* **32**(L03302), doi:10.1029/2004GL021793.

Dunham, E.M., Belanger, D., Cong, L. & Kozdon, J.E., 2011. Earthquake ruptures with strongly rate-weakening friction and off-fault plasticity, part 2: nonplanar faults, *Bull. seism. Soc. Am.,* **101**(5), 2308–2322.

Flatté, S.M. & Wu, R.S., 1988. Small-scale structure in the lithosphere and asthenosphere deduced from arrival time and amplitude fluctuations at NORSAR, *J. geophys. Res.,* **93**(B6), 6601–6614.

Fletcher, J.B., Spudich, P. & Baker, L.M., 2006. Rupture propagation of the 2004 Parkfield, California, earthquake from observations at the UPSAR, *Bull. seism. Soc. Am.,* **96**(4), S129–S142.

Frankel, A. & Clayton, R.W., 1986. Finite-difference simulations of seismic scattering—implications for the propagation of short-period seismic-waves in the crust and models of crustal heterogeneity, *J. geophys. Res.,* **91**(B6), 6465–6489.

Frenje, L. & Juhlin, C., 2000. Scattering attenuation: 2D and 3D finite difference simulations vs. theory, *J. appl. Geophys.,* **44**(1), 33–46.

Goff, J. & Holliger, K., 1999. Nature and origin of upper crustal seismic velocity fluctuations and associated scaling properties- combined stochastic analyses of KTB velocity and lithology logs, *J. geophys. Res.,* **104**(B6), 169–182.

Graves, R.W. & Pitarka, A., 2010. Broadband ground-motion simulation using a hybrid approach, *Bull. seism. Soc. Am.,* **100,** 2095.

Guatteri, M., Mai, P.M., Beroza, G.C. & Boatwright, J., 2003. Strong ground-motion prediction from stochastic-dynamic source models, *Bull. seism. Soc. Am.,* **93**(1), 301–313.

Gusev, A.A. & Abubakirov, I.R., 1996. Simulated envelopes of non-isotropically scattered body waves as compared to observed ones: another manifestation of fractal heterogeneity, *Geophys. J. Int.,* **127**(1), 49–60.

Hao, H., Oliveira, C.S. & Penzien, J., 1989. Multiple-station ground motion processing and simulation based on SMART-1 array data, *Nucl. Eng. Des.,* **111**(3), 293–310.

Harichandran, R.S. & Vanmarcke, E.H., 1986. Stochastic variation of earthquake ground motion in space and time, *J. Eng. Mech-Asce,* **112**(2), 154–174.

Hartzell, S., Harmsen, S. & Frankel, A., 2010. Effects of 3D random correlated velocity perturbations on predicted ground motions, *Bull. seism. Soc. Am.,* **100**(4), 1415–1426.

Hedlin, M.A.H., Shearer, P.M. & Earle, P.S., 1997. Seismic evidence for small-scale heterogeneity throughout the earth's mantle, *Nature,* **387**(6629), 145–150.

Helffrich, G.R. & Wood, B.J., 2001. The earth's mantle, *Nature,* **412,** 501–507.

Holliger, K., 1996. Upper-crustal seismic velocity heterogeneity as derived from a variety of P-wave sonic logs, *Geophys. J. Int.,* **125**(3), 813–829.

Holliger, K., 1997. Seismic scattering in the upper crystalline crust based on evidence from sonic logs, *Geophys. J. Int.,* **128**(1), 65–72.

Holliger, K. & Levander, A.R., 1992. A stochastic view of lower crustal fabric based on evidence from the Ivrea zone, *Geophys. Res. Lett.,* **19**(11), 1153–1156.

Imperatori, W. & Mai, P.M., 2012. Sensitivity of broad-band ground-motion simulations to earthquake source and Earth structure variations: an application to the Messina Straits (Italy), *Geophys. J. Int.,* **188**(3), 1103–1116.

Levander, A., Hobbs, R.W., Smith, S.K., England, R.W., Snyder, D.B. & Holliger, K., 1994. The crust as a heterogeneous optical medium, or crocodiles in the mist, *Tectonophysics,* **232**(1-4), 281–297.

Levander, A.R. & Holliger, K., 1992. Small-scale heterogeneity and large-scale velocity structure of the continental-crust, *J. geophys. Res.,* **97**(B6), 8797–8804.

L'heureux, E., Milkereit, B. & Vasudevan, K., 2009. Heterogeneity and seismic scattering in exploration environments, *Tectonophysics,* **472**(1–4), 264–272.

Liu, H.L. & Helmberger, D.V., 1985. The 23-19 aftershock of the 15 October 1979 Imperial Valley earthquake—more evidence for an asperity, *Bull. seism. Soc. Am.,* **75**(3), 689–708.

Liu, P., Archuleta, R.J. & Hartzell, S.H., 2006. Prediction of broadband ground-motion time histories: hybrid low/high-frequency method with correlated random source parameters, *Bull. seism. Soc. Am.,* **96**(6), 2118–2130.

Mai, P.M., 2009. Ground-motion complexity and scaling in the near-field of earthquake ruptures, in *Encyclopedia of Complexity and System Sciences,* pp. 4435–4474, eds Lee, W. & Meyers, R., Springer, New York.

Mai, P.M., Imperatori, W. & Olsen, K.B., 2010. Hybrid broadband ground-motion simulations: combining long-period deterministic synthetics with high-frequency multiple S-to-S backscattering, *Bull. seism. Soc. Am.,* **100**(5A), 2124–2142.

Martini, F, Bean, C.J., Dolan, S. & Marsan, D., 2001. Seismic image quality beneath strongly scattering structures and implications for lower crustal imaging: numerical simulations, *Geophys. J. Int.,* **145,** 423–435.

Mayeda, K., Koyanagi, S., Hoshiba, M., Aki, K. & Zeng, Y.H., 1992. A comparative-study of scattering, intrinsic, and coda Q^{-1} for Hawaii, Long Valley, and central California between 1.5 Hz and 15.0 Hz, *J. geophys. Res.,* **97**(B5), 6643–6659.

Mena, B., Mai, P.M., Olsen, K.B., Purvance, M.D. & Brune, J.N., 2010. Hybrid broadband ground-motion simulation using scattering Green's functions: application to large-magnitude events, *Bull. seism. Soc. Am.,* **100**(5A), 2143–2162.

Mossessian, T.K. & Dravinski, M., 1990. Amplification of elastic-waves by a 3-dimensional valley. 1. Steady-state response, *Earthq. Eng. Struc.,* **19**(5), 667–680.

Nielsen, L. & Thybo, H., 2003. The origin of teleseismic Pn waves: multiple crustal scattering of upper mantle whispering gallery phases, *J. geophys. Res.,* **108**(B10), doi:10.1029/2003JB002487.

Nielsen, L. & Thybo, H., 2006. Identification of crustal and upper mantle heterogeneity by modelling of controlled-source seismic data, *Tectonophysics,* **416**(1–4), 209–228.

Olsen, K.B. *et al.*, 2009. Shakeout-D: ground motion estimates using an ensemble of large earthquakes on the southern San Andreas Fault with spontaneous rupture propagation, *Geophys. Res. Lett.,* **36,** L04 303.

Pardoiguzquiza, E. & Chicaolmo, M., 1993. The Fourier integral method—an efficient spectral method for simulation of random-fields, *Math. Geol.,* **25**(2), 177–217.

Pitarka, A., 2009. Simulating forward and backward scattering in viscoelastic 3D media with random velocity variations and basin structure, *Tech. Rep.,* USGS, award number 06HQGR0042.

Przybilla, J., Korn, M. & Wegler, U., 2006. Radiative transfer of elastic waves versus finite difference simulations in two-dimensional random media, *J. geophys. Res.,* **111**(B04305), doi:10.1029/2005JB003952.

Przybilla, J., Wegler, U. & Korn, M., 2009. Estimation of crustal scattering parameters with elastic radiative transfer theory, *Geophys. J. Int.,* **178**(2), 1105–1111.

Pulido, N. & Dalguer, L.A., 2009. Estimation of the high-frequency radiation of the 2000 Tottori (Japan) earthquake based on a dynamic model of fault rupture: application to the strong ground motion simulation, *Bull. seism. Soc. Am.,* **99**(4), 2305–2322.

Pulido, N. & Kubo, T., 2004. Near-fault strong motion complexity of the 2000 Tottori earthquake (Japan) from a broadband source asperity model, *Tectonophysics,* **390**(1–4), 177–192.

Ripperger, J., Mai, P.M. & Ampuero, J.P., 2008. Variability of near-field ground motion from dynamic earthquake rupture simulations, *Bull. seism. Soc. Am.,* **98**(3), 1207–1228.

Roth, M. & Korn, M., 1993. Single scattering-theory versus numerical modeling in 2D random-media, *Geophys. J. Int.,* **112**(1), 124–140.

Saito, T., Sato, H. & Ohtake, M., 2002. Envelope broadening of spherically outgoing waves in three-dimensional random media having power law spectra, *J. geophys. Res.,* **107**(B5), doi:10.1029/2001JB000264.

Sato, H., 1977. Single isotropic scattering model including wave conversions simple theoretical model of the short period body wave propagation, *J. Phys. Earth*, **25,** 163–176.

Sato, H., 1989. Broadening of seismogram envelopes in the randomly inhomogeneous lithosphere based on the parabolic approximation—southeastern Honshu, Japan, *J. geophys. Res.,* **94**(B12), 17 735–17 747.

Sato, H. & Fehler, M.C., 1994. *Seismic Wave Propagation and Scattering in the Heterogeneous Earth,* AIP Springer, New York.

Sawazaki, K., Sato, H. & Nishimura, T., 2011. Envelope synthesis of short-period seismograms in 3D random media for a point shear dislocation source based on the forward scattering approximation: application to small strike-slip earthquakes in southwestern Japan, *J. geophys. Res.,* **116**(B08305), doi:10.1029/2010JB008182.

Schneider, J., Stepp, J. & Abrahamson, N., 1992. The spatial variation of earthquake ground motion and effects of local site conditions, in *Proceedings of the Tenth World Conference on Earthquake Engineering*, Rotterdam.

Shapiro, S.A. & Kneib, G., 1993. Seismic attenuation by scattering—theory and numerical results, *Geophys. J. Int.,* **114**(2), 373–391.

Somerville, P., Smith, N. & Abrahamson, R.G.N., 1997. Modification of empirical strong ground motion attenuation relations to include the amplitude and duration effects of rupture directivity, *Seismol. Res. Lett.,* **68**(1), 199–222.

Sørensen, M.B., Pulido, N. & Atakan, K., 2007. Sensitivity of ground-motion simulations to earthquake source parameters: a case study for Istanbul, Turkey, *Bull. seism. Soc. Am.,* **97**(3), 881–900.

Spudich, P. & Chiou, B.S.J., 2008. Directivity in NGA earthquake ground motions: analysis using isochrone theory, *Earthq. Spectra,* **24**(1), 279–298.

Stein, S. & Wysession, M., 2003. *An Introduction to Seismology, Earthquakes, and Earth Structure,* Vol. 56, Blackwell Publishing.

Takemura, S., Furumura, T. & Saito, T., 2009. Distortion of the apparent S-wave radiation pattern in the high-frequency wavefield: Tottori-Ken Seibu, Japan, earthquake of 2000, *Geophys. J. Int.,* **178**(2), 950–961.

Takenaka, H., Mamada, Y. & Futamure, H., 2003. Near-source effect on radiation pattern of high-frequency S waves: strong SH-SV mixing observed from aftershocks of the 1997 northwestern Kagoshima, Japan, earthquakes, *Phys. Earth planet. Inter.,* **137**(1–4), 31–43.

Tan, Y. & Helmberger, D., 2010. Rupture directivity characteristics of the 2003 Big Bear sequence, *Bull. seism. Soc. Am.,* **100**(3), 1089–1106.

Thybo, H., Nielsen, L. & Perchuc, E., 2003. Seismic scattering at the top of the mantle transition zone, *Earth planet. Sci. Lett.,* **216**(3), 259–269.

Vidale, J.E., 1989. Influence of focal mechanism on peak accelerations of strong motions of the Whittier-Narrows, California, earthquake and an aftershock, *J. geophys. Res.,* **94**(B7), 9607–9613.

Wu, R.S., 1985. Multiple-scattering and energy-transfer of seismic-waves separation of scattering effect from intrinsic attenuation .1. Theoretical modeling, *Geophys. J. R. astr. Soc.,* **82**(1), 57–80.

Wu, R.S. & Aki, K., 1988. Seismic-wave scattering in 3-dimensionally heterogeneous earth—introduction, *Pure appl. Geophys.,* **128**(1–2), 1–6.

Zeng, Y.H., 1991. Compact solutions for multiple scattered wave energy in time domain, *Bull. seism. Soc. Am.,* **81**(3), 1022–1029.

Zeng, Y.H., 1993. Theory of scattered P-wave and S-wave energy in a random isotropic scattering medium, *Bull. seism. Soc. Am.,* **83**(4), 1264–1276.

Zeng, Y.H., Su, F. & Aki, K., 1991. Scattering wave energy propagation in a random isotropic scattering medium .1. theory, *J. geophys. Res.,* **96**(B1), 607–619.

Zeng, Y.H., Anderson, J.G. & Su, F., 1995. Subevent rake and random scattering effects in realistic strong ground motion simulation, *Geophys. Res. Lett.,* **22**(1), 17–20.

Zerva, A. & Zervas, V., 2002. Spatial variation of seismic ground motions: an overview, *Appl. Mech. Rev.,* **55**(3), 271–297.

SUPPORTING INFORMATION

Additional Supporting Information may be found in the online version of this article:

(http://gji.oxfordjournals.org/lookup/supp1/doi:10.1093/gji/ggs041/-/DC1).

Please note: Oxford University Press are not responsible for the content or functionality of any supporting materials supplied by the authors. Any queries (other than missing material) should be directed to the corresponding author for the article.